

Electronic Structures of Active Sites in Copper Proteins and Their Contributions to Reactivity

Edward I. Solomon, Michael D. Lowery, David E. Root,
and Brooke L. Hemming

Department of Chemistry, Stanford University, Stanford, CA 94305

Many active sites in copper proteins exhibit unique spectral features in comparison to small inorganic complexes. These spectral features are becoming well-understood and reflect unusual electronic structures that make key contributions to the reactivity of these sites in biology. In blue copper proteins, the unique spectral features reflect a ground-state, redox-active wave function that has high anisotropic covalency involving a cysteine ligand that activates this residue for rapid, directional, long-range electron transfer. For hemocyanin and tyrosinase, the characteristic spectral features reflect a peroxide-binuclear cupric bond that has very strong σ -donor and π -acceptor interactions that stabilize the oxy site with respect to loss of peroxide. In tyrosinase, this bonding mode activates peroxide for hydroxylation of phenolic substrates by making the peroxide less negative but with an unusually weak O–O bond. Finally, for the multicopper oxidases, magnetic circular dichroism and X-ray absorption studies first showed the presence of a trinuclear copper cluster site, which is the minimal structural unit required for the multielectron reduction of dioxygen to water. A peroxide level intermediate in this reduction has been obtained and is found to have strikingly different spectral features than those associated with bound peroxide in oxyhemocyanin and oxytyrosinase. This demonstrates a fundamentally different electronic and geometric structure for peroxide binding in the multicopper oxidases that promotes the further reduction of peroxide to water at the trinuclear copper cluster site.

MANY CLASSES OF ACTIVE SITES in copper proteins exhibit unique spectral features when compared to simple, high-symmetry transition-

0065-2393/95/0246-0121/\$12.32/0
© 1995 American Chemical Society

metal complexes. These active sites derive from the unusual geometric and electronic structures that can be imposed on the metal ion in a protein environment. It has been a general goal of our research to understand these electronic structures and to evaluate their contributions to the reactivities of these active sites in catalysis (1–3).

Our progress in four areas will be summarized (4, 5). First, if one is to understand the origin of these unique spectral features, one must understand the electronic structure of “normal” high-symmetry, transition-metal complexes. Square-planar cupric chloride has served as an electronic structural model complex and is now one of the best understood molecules in inorganic chemistry (6). Its spectral features and the electronic structure these reflect will be briefly described in the following section (4). Having provided this description of a “normal” copper site, the unique spectral features of the blue copper active site will then be addressed. An understanding of these features provides insight into ground and excited state contributions to the rapid rate of long-range electron transfer observed in this family of proteins. Next we focus on the coupled binuclear copper proteins, hemocyanin, and tyrosinase. These proteins have similar active sites that generate the same oxy intermediate involving peroxide bound to two copper(II) ions. The hemocyanins reversibly bind dioxygen and function as oxygen carriers in arthropods and molluscs, whereas the tyrosinases have highly accessible active sites that bind phenolic substrates and oxygenate them to *ortho*-diphenols. Their oxy sites exhibit unique excited state spectral features that reflect novel peroxide–copper bonding interactions that make a significant electronic contribution to the binding and activation of dioxygen by these sites. In the final section, spectroscopic studies of the multicopper oxidases, which include laccase, ascorbate oxidase, and ceruloplasmin, are summarized. These enzymes catalyze the four-electron reduction of dioxygen to water. Spectral studies have demonstrated that the multicopper oxidases contain a fundamentally different coupled binuclear copper site (called type 3) when compared with hemocyanin and tyrosinase. The type 3 site is part of a trinuclear copper cluster that plays the key role in the multielectron reduction of dioxygen by this important class of enzymes.

Normal Copper Complexes

Placing a cupric ion with its nine *d* electrons in an octahedral ligand field produces a 2E_g ground state (Figure 1). This ground state is unstable to a Jahn–Teller distortion that lowers the symmetry and energy of the complex. The Jahn–Teller distortion normally observed is a tetragonal elongation along the *z*-axis and contraction in the equatorial *x,y* plane that ultimately results in a square-planar ligand environment as in D_{4h} .

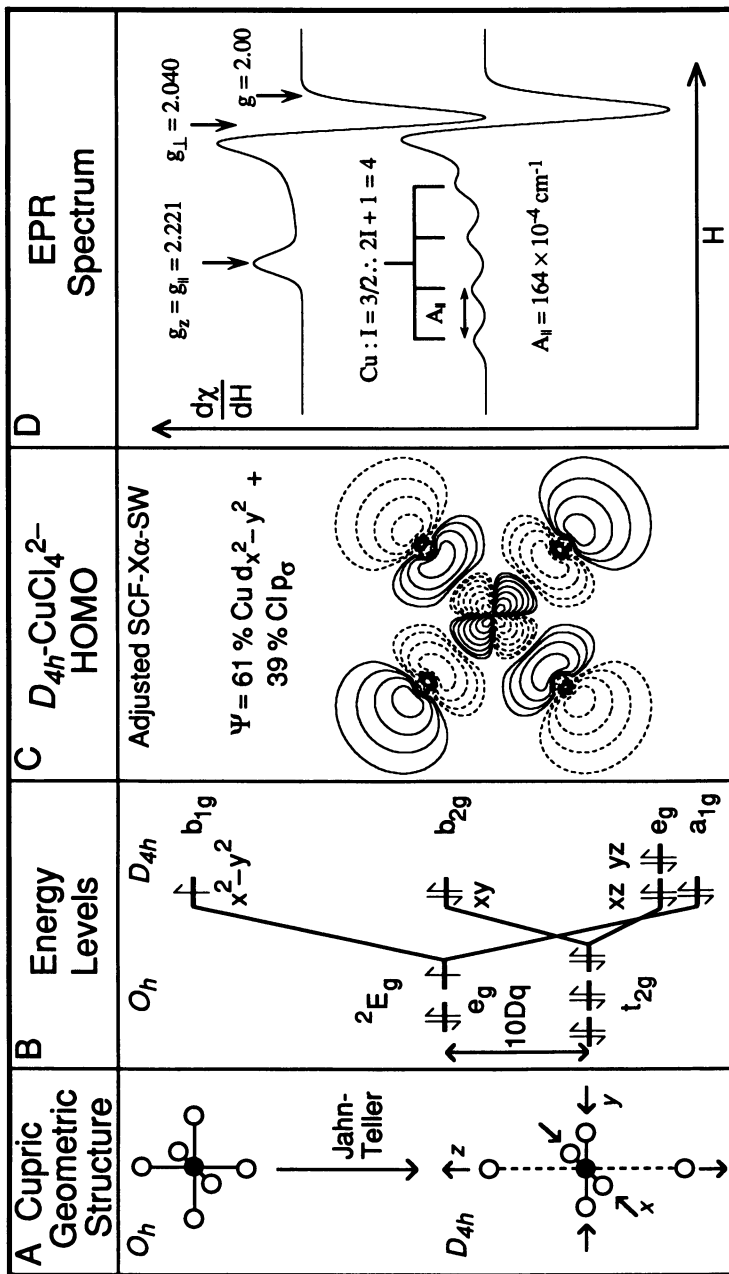


Figure 1. The ground-state spectral features of normal copper complexes. A: Jahn-Teller tetragonal elongation of an octahedral CuL₆ complex to the square planar limit. B: Energy level correlation diagram for the Jahn-Teller distortion depicted in A. C: SCF-Xα-SW wave function contour and charge decomposition for the HOMO of D_{4h}-CuCl₄²⁻ (18, 19). D: X-band EPR spectrum for tetragonal Cu(II) with D_{4h}-CuCl₄²⁻ parameters.

CuCl_4^{2-} (Figure 1A). A key feature of ligand field theory (7–11) is that the d orbital splitting is very sensitive to the environment of the ligands around the metal center. The d orbital splitting experimentally determined using optical spectroscopy (12) for D_{4h} - CuCl_4^{2-} is given in Figure 1B. The half-occupied $d_{x^2-y^2}$ orbital is at highest energy as it has the largest repulsive interaction with the ligands in the equatorial plane. A more complete description of this half-occupied ground state is provided by molecular orbital (MO) theory. In particular, self-consistent field-X α -scattered wave (SCF-X α -SW) calculations (13–17), adjusted to ground-state parameters (18–21) as will be described, are in good agreement with spectral data over many orders of magnitude in energy. These calculations (18, 19) generate a description of the ground state of D_{4h} - CuCl_4^{2-} that has 61% Cu $d_{x^2-y^2}$ character with the remaining part of the wave function being delocalized equivalently into the four $p\sigma$ orbitals of the chloride ligands that are involved in antibonding interactions with the metal ion (Figure 1C). The unpaired electron in this wave function produces the electron paramagnetic resonance (EPR) spectrum shown in Figure 1D, in which $g_{||}$ (corresponding to the magnetic field oriented along the z -axis of the complex) $> g_{\perp} > 2.00$, that is characteristic of this $d_{x^2-y^2}$ ground state. Additionally, copper has a nuclear spin ($I_N = \frac{3}{2}$) that couples to the electron spin to produce a four-line hyperfine splitting (A) of the EPR spectrum. Tetragonal cupric complexes generally have a large hyperfine splitting in the $g_{||}$ region ($A_{||} > 130 \times 10^{-4} \text{ cm}^{-1}$); that of D_{4h} - CuCl_4^{2-} is $164 \times 10^{-4} \text{ cm}^{-1}$ (22).

With respect to excited states, optical excitation of electrons from the filled Cu d orbitals to the half-filled $d_{x^2-y^2}$ orbital (Figure 2A) produces Laporté-forbidden ligand-field transitions (23). These transitions are weak in the absorption spectrum with molar extinction coefficients (ϵ) of $30\text{--}50 \text{ M}^{-1} \text{ cm}^{-1}$ in the $12,000\text{--}16,000 \text{ cm}^{-1}$ region (12) (Figure 2B, right). Observed at higher energy in the absorption spectrum are the Laporté-allowed ligand-to-metal charge-transfer transitions that are at least two orders of magnitude more intense than the ligand-field transitions (24) (Figure 2B, left). The energies and intensities of these charge-transfer (CT) transitions allow one to probe the specific bonding interactions of the ligand with the metal center (24). Chloride has three valence $3p$ orbitals that split into two sets on binding to copper (Figure 2C). The $p\sigma$ orbital is oriented along the Cl–Cu bond and is stabilized to higher binding energy due to strong overlap with the Cu^{2+} ion. The two chloride $p\pi$ orbitals are perpendicular to the Cl–Cu bond and hence are more weakly interacting with the metal and at lower binding energy.

The intensity associated with charge-transfer excitation of an electron from these filled ligand orbitals into the half-occupied Cu $d_{x^2-y^2}$ orbital also reflects metal–ligand bonding. Charge-transfer intensity is proportional to $(RS)^2$, where S is the overlap of the donor and acceptor

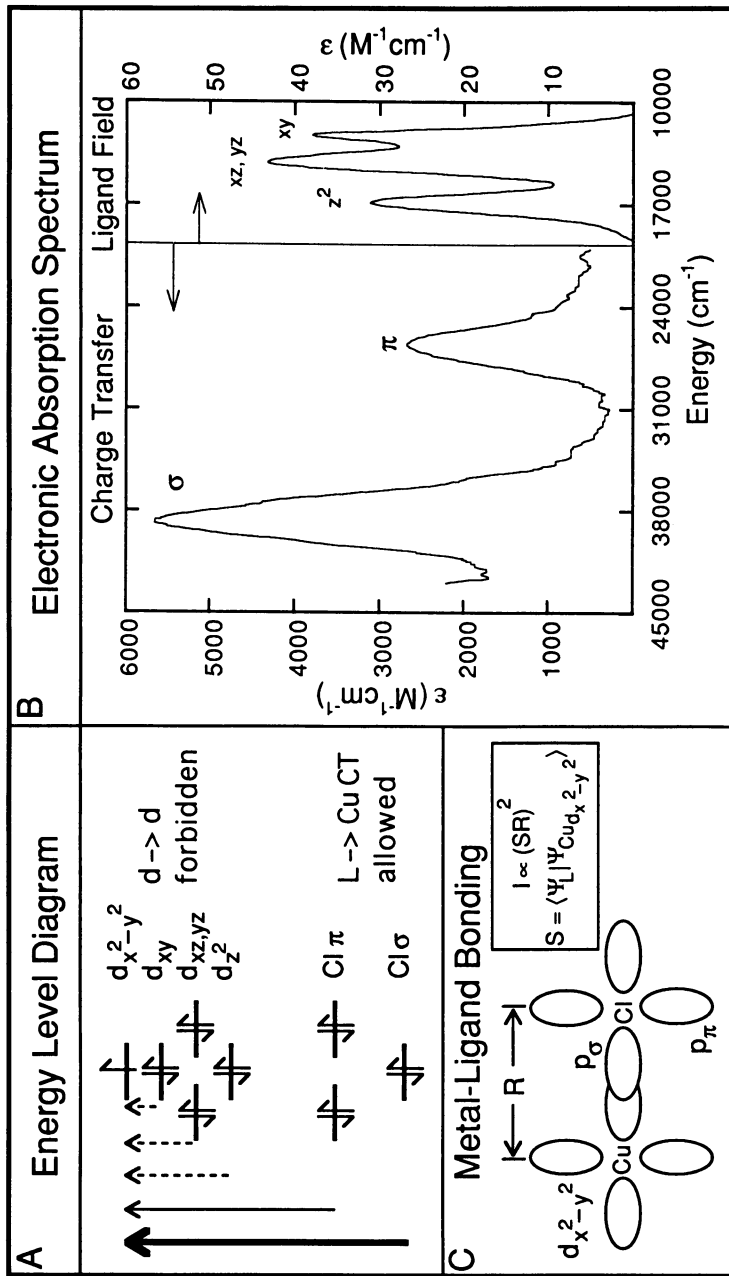


Figure 2. Excited-state spectral features of $D_{4h}\text{-CuCl}_4^{2-}$. A: Energy level diagram showing the ligand-field ($d \rightarrow d$) and charge-transfer (CT) optical transitions. The intensity of the transitions is approximated by the thickness of the arrow with the very weak ligand-field transitions represented as a dotted arrow. B: Electronic absorption spectrum for $D_{4h}\text{-CuCl}_4^{2-}$ (12). C: Schematic of the σ and π bonding modes between the Cu $3d_{x^2-y^2}$ and Cl $3p$ orbitals.

orbitals involved in the charge-transfer transition and R is the metal-ligand bond length (25). Thus, the Cl $p\sigma \rightarrow \text{Cu } d_{x^2-y^2}$ charge-transfer transition is at high energy and intense from large overlap, while the Cl $p\pi \rightarrow d_{x^2-y^2}$ charge transfer transition is at lower energy and weaker (Figure 2C). (Note that the ligand orbitals are actually linear combinations of the orbitals from the four chloride ligands. One combination of the Cl $p\sigma$ orbitals has e_u symmetry. The CT transition from this orbital is electric dipole allowed and responsible for the intense band at 36,000 cm^{-1} . The Cl $p\pi$ set also contains a linear combination having e_u symmetry. Configurational interaction with $e_u(p\sigma)$ contributes to the intensity of the $p\pi \rightarrow d_{x^2-y^2}$ band at 26,500 cm^{-1}). The key points to be emphasized here are that the charge-transfer transitions sensitively probe the ligand-metal bond and that for “normal” complexes one should observe a lower-energy weak π and higher-energy intense σ charge-transfer transition as is observed experimentally for CuCl_4^{2-} in Figure 2B (left).

Blue Copper Proteins

As predicted by spectroscopy (26), the blue copper site has a structure very different from the normal tetragonal geometry of cupric complexes. The copper site in plastocyanin (27) has a distorted tetrahedral structure with a thiolate sulfur of cysteine (Cys) 84 bound with a short Cu–S bond length of 2.13 Å, a thioether sulfur of methionine (Met) 92 bound with a long Cu–S bond length of 2.90 Å, and two fairly normal histidine (His) N–Cu ligands (Figure 3A). This site has characteristic spectral features (1–3) that include an intense absorption band ($\epsilon \sim 3,000\text{--}5,000 \text{ M}^{-1} \text{ cm}^{-1}$) in the 600 nm ligand-field region (Figure 3B) and a small parallel hyperfine splitting ($A_{||} \leq 70 \times 10^{-4} \text{ cm}^{-1}$) (Figure 3C). These unusual spectral features are now well-understood and help to define the ground-state wave function of the blue copper site. This is extremely important in that this is the half-occupied orbital that takes up and transfers the electron in the redox functioning of this center. A detailed experimental and theoretical description of the ground state provides fundamental insight into the active site contribution to the long-range electron-transfer reactivity exhibited by the blue copper proteins (2, 3, 28).

The EPR spectrum of the blue copper protein plastocyanin (Figure 3C) has $g_{||} > g_{\perp} > 2.00$, and thus the copper site must have a $d_{x^2-y^2}$ ground state. First, we are interested in determining the orientation of the $d_{x^2-y^2}$ orbital relative to the distorted tetrahedral geometry observed in the protein crystal structure. Single crystal EPR spectroscopy allowed us to obtain this orientation and located the unique (i.e., z) direction in this distorted site (29). Plastocyanin crystallizes in an orthorhombic space group with four symmetry related molecules in the unit cell. The orientation of the plastocyanin copper sites in the unit cell are shown in

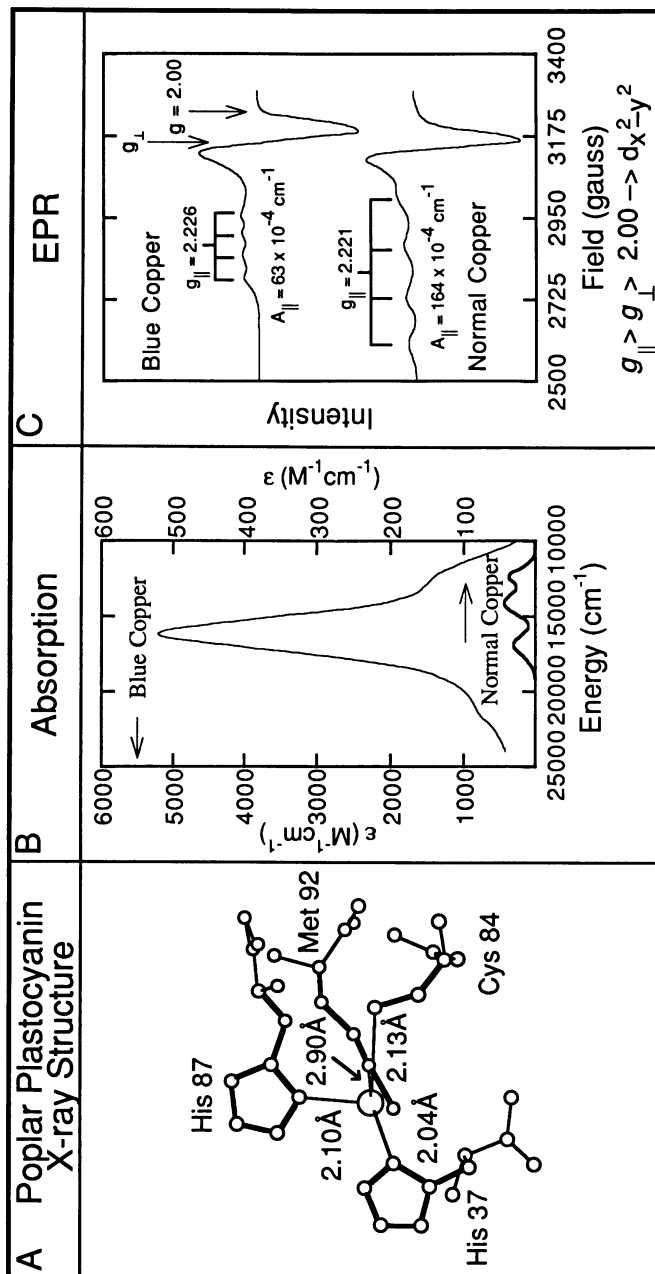


Figure 3. Blue copper proteins. A: X-ray structure of poplar plastocyanin (27). B: Absorption spectrum of plastocyanin and ‘normal’ $\text{D}_{4h}\text{-CuCl}_4^{2-}$ (ϵ scale expanded by 10). C: X-band EPR spectrum of plastocyanin and $\text{D}_{4h}\text{-CuCl}_4^{2-}$.

Figure 4A (27). Figure 4B presents the EPR spectra obtained if one rotates the crystal around the *a* axis with the magnetic field in the *b/c* plane. The key feature to note in the figure is that one observes an $\sim g_{\parallel}$ EPR signal (with four parallel hyperfine components) with the field along the *c* axis and an $\sim g_{\perp}$ spectrum as the field is rotated perpendicular to this direction. Thus, g_{\parallel} is nearly colinear with the *c* axis. Referencing to the four blue copper sites in the unit cell, each has its Met S–Cu bond approximately along the *c* axis. Therefore, g_{\parallel} is approximately along the long Met S–Cu bond. A more quantitative fit of the EPR data shows that g_{\parallel} , which defines the *z*-axis of the site, is $\sim 5^\circ$ off the Met S–Cu bond and places the $d_{x^2-y^2}$ orbital perpendicular to this direction and within 15° of the plane defined by the thiolate S and two imidazole N ligands.

The next feature of the ground-state wave function to be discussed is the origin of the small parallel hyperfine splitting ($A_{\parallel} < 70 \times 10^{-4}$ cm $^{-1}$). Distorted tetrahedral cupric sites, for example $D_{2d}\text{-CuCl}_4^{2-}$, often exhibit small A_{\parallel} values similar to the blue copper proteins and the mechanism for reducing the parallel hyperfine value has been thought to have a common origin. In $D_{2d}\text{-CuCl}_4^{2-}$, the small A_{\parallel} value has been attributed to the effect of Cu 4p mixing into the $d_{x^2-y^2}$ orbital, which is allowed in lower-symmetry metal sites (30). In D_{2d} symmetry, the $4p_z$ orbital is allowed by group theory to mix into the $d_{x^2-y^2}$ orbital. The spin dipolar interaction of the $4p_z$ orbital with the copper nuclear spin opposes that of the electron spin in the $d_{x^2-y^2}$ orbital and reduces the A_{\parallel} value (4p mixing is forbidden in D_{4h} -symmetry). Twelve percent 4p_{*z*} mixing is required to lower the A_{\parallel} value to that value observed for $D_{2d}\text{-CuCl}_4^{2-}$ and plastocyanin (31, 32).

The nature of the 4p mixing into the $d_{x^2-y^2}$ orbital of plastocyanin is determined by the effective symmetry of the ligand field of the active site. A combination of low-temperature magnetic circular dichroism (LT-MCD) spectroscopy (33) and ligand field theory (29) has been used to obtain the splitting of the *d* orbitals of the blue copper site. Five non-degenerate ligand-field levels are observed indicating a rhombically distorted site (Figure 5B, left); however, the splitting is close to an axial limit. The *d* orbital splitting for the axial limit (Figure 5B, right) corresponds to a C_{3v} axially elongated tetrahedral structure in which the *z*-axis corresponds to the long thioether S–Cu bond (Figure 5C). However, in C_{3v} symmetry, the $d_{x^2-y^2}$ orbital is only allowed to mix with the $4p_x$, $4p_y$ levels and, in this case, the spin dipolar interactions would be complementary and increase the A_{\parallel} value.

Thus we needed to determine experimentally the nature of the 4p mixing into the $d_{x^2-y^2}$ level. This determination was accomplished by going up about 10 orders of magnitude in photon energy and performing X-ray absorption spectroscopy (XAS) at the Cu-K edge (34). The 8979-eV pre-edge peak, corresponding to the Cu 1s \rightarrow $3d_{x^2-y^2}$ transition, can

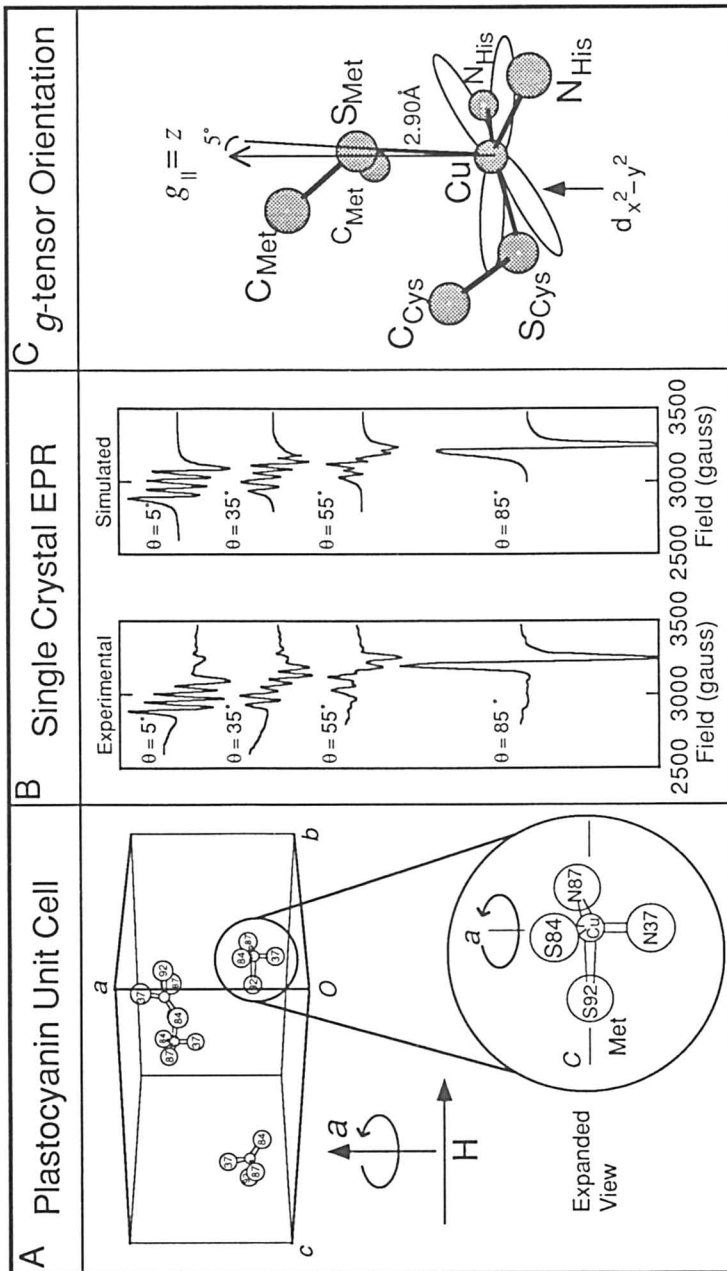


Figure 4. Single-crystal EPR of poplar plastocyanin (29); orientation of the $d_{x^2-y^2}$ orbital. A: Unit cell and molecular orientation with respect to the applied magnetic field. B: EPR spectra and simulations for the crystal orientations shown. C: Orientation of the g_{\parallel} direction and the $d_{x^2-y^2}$ orbital superimposed on the blue copper site.

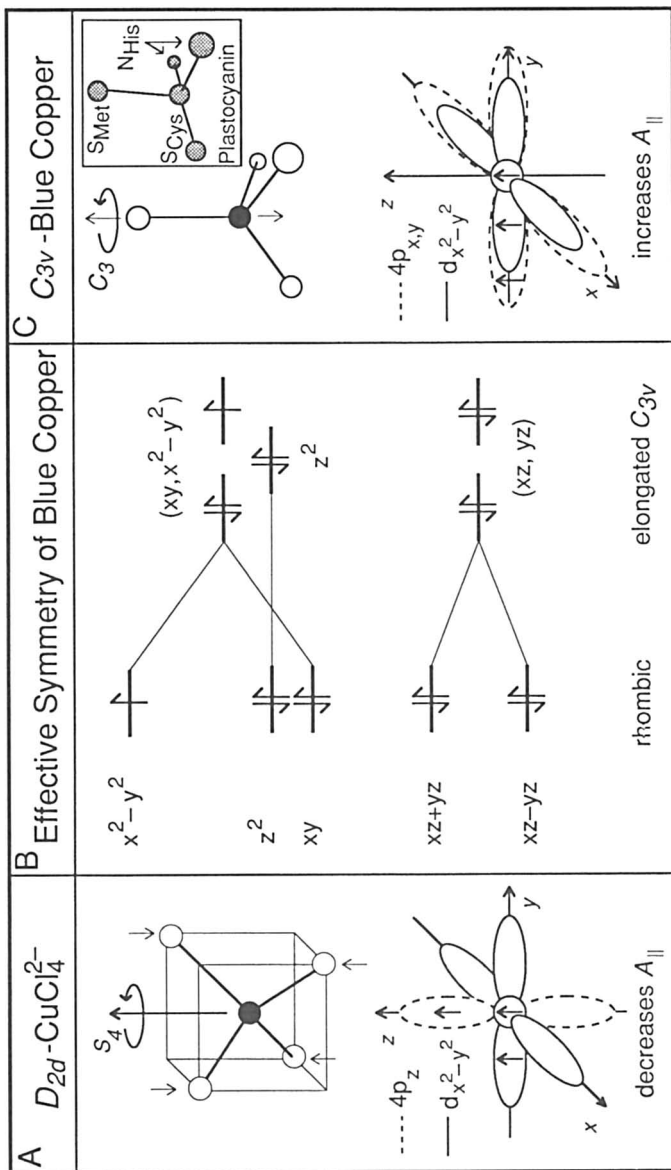


Figure 5. Origin of small $A_{||}$ values (34). A: $4p_z$ mixing with the $d_{x^2-y^2}$ orbital in D_{2d} symmetry lowers $A_{||}$. B: Energy levels for blue copper site (left) and its axial C_{3v} limit (right). C: Effect of $4p_{x,y}$ mixing with the $d_{x^2-y^2}$ orbital on $A_{||}$ for a C_{3v} distortion.

have no electric dipole intensity unless the copper site is distorted such that some Cu $4p$ orbital character mixes into the half-occupied $d_{x^2-y^2}$ level (Figure 6A). The intensity of the 8979-eV feature is much higher in the plastocyanin and D_{2d} -CuCl₄²⁻ edges relative to the square planar D_{4h} -CuCl₄²⁻ complex (34). This higher intensity indicates the presence of $4p$ mixing in the $d_{x^2-y^2}$ orbitals of plastocyanin and D_{4h} -CuCl₄²⁻ (Figure 6B). It was then important to determine whether the $4p$ mixing in the blue copper site involves the p_z or p_x, p_y orbitals. This may be accomplished through analysis of the polarized single crystal X-ray absorption spectra of plastocyanin. The single crystal EPR data (29) determined the z -axis as being approximately colinear with the long thioether S-Cu bond. Polarized edge data were obtained (35) with the E vector of light parallel and perpendicular to this direction. No 8979-eV intensity was observed for $E_{\parallel} z$, requiring that there is no $4p_z$ mixing, whereas all the 8979-eV intensity was observed in the $E_{\parallel} x, y$ spectrum. Thus, only Cu $4p_z, p_y$ mixes into the $d_{x^2-y^2}$ orbital of plastocyanin and the small A_{\parallel} value of the blue copper site cannot be due to the generally accepted mechanism of $4p_z$ mixing.

Having eliminated $4p_z$ mixing, we can focus on the alternative explanation for the small A_{\parallel} value of the blue copper site that is covalent delocalization of the electron spin onto the ligands (33, 36). Covalency reduces the hyperfine interaction of the unpaired electron with the copper nuclear spin. We have approached the inclusion of covalency in the description of the ground state of the blue copper site through a quantitative consideration of its g values. Multifrequency EPR spectroscopy (36) gives the experimental g values for plastocyanin listed on the left in Table I. If the ground state only involves an unpaired electron in a $d_{x^2-y^2}$ orbital, there would only be a spin angular momentum contribution to the g values and thus the g values would be 2.00 and isotropic. Ligand field theory (LFT) (7–11) allows for the inclusion of some orbital angular momentum into the $d_{x^2-y^2}$ ground state through its spin-orbit mixing with ligand-field excited states. This orbital contribution leads to the devia-

Table I. Blue Copper Covalency → Quantitative Analysis of g Values

g	<i>Plastocyanin Experimental</i>	(x^2-y^2) <i>Spin Only</i>	<i>LFT d Orbitals + $\lambda L \cdot S$</i>	<i>SCF-Xα-SW d Levels, CT Levels $\lambda_{Cu} L \cdot S + \lambda_L L \cdot S$</i>	
				<i>Normal Radii</i>	<i>Adjusted Radii</i>
g_x	2.047	2.00	2.125	2.046	2.059
g_y	2.059	2.00	2.196	2.067	2.076
g_z	2.226	2.00	2.479	2.159	2.226

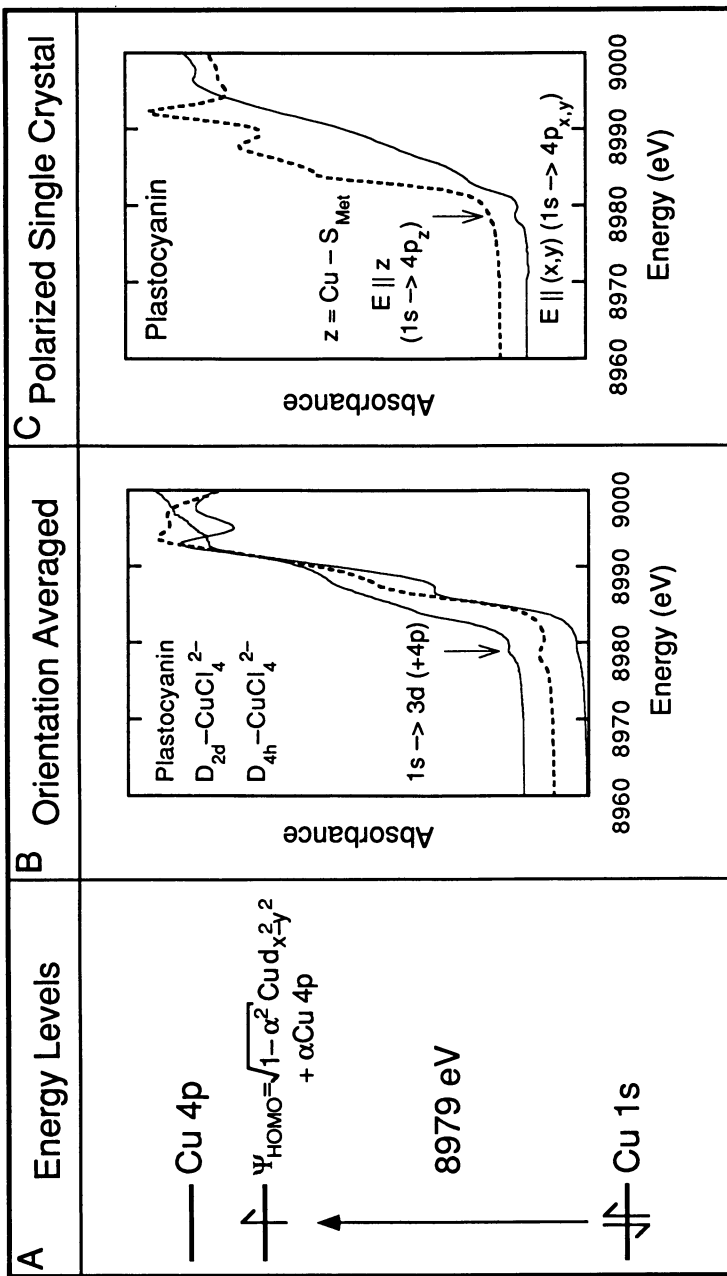


Figure 6. X-ray absorption spectroscopy. A: Energy level diagram depicting a Cu 1s → HOMO transition at ~8979 eV. B: Orientation averaged XAS spectra. C: Polarized single-crystal XAS spectra for poplar plastocyanin. (Data are from reference 35.)

tions of the g values from 2.00. A complete ligand-field calculation for plastocyanin gives the g values listed in the third column of Table I. Here, $g_{\parallel} > g_{\perp} > 2.00$, which is consistent with a spin-orbit mixed $d_{x^2-y^2}$ ground state. However, the calculated values are larger than the experimental values. This is due to the fact that the ligand field calculations use pure d orbitals that have too much orbital angular momentum. Covalent delocalization of the unpaired electron onto the ligands reduces the orbital contribution to the g values.

SCF-X α -SW calculations (33, 36) were pursued to describe the bonding in the blue copper site. The wave functions obtained from these calculations were used to calculate the ground state g values and evaluate the covalent description generated by these calculations relative to experiment. The g value calculation included all the antibonding (d) and bonding (charge transfer) levels and included spin-orbit mixing from both the metal and the ligands. A Zeeman operator was applied to the spin-orbit corrected ground state making no assumption concerning the orientation of the principal axes. A g^2 tensor was generated and diagonalized to obtain the principal component g values that can be compared to experiment (fourth column). It is observed that although the g values are reduced from those obtained from the ligand-field calculation due to the inclusion of covalency, they are closer to 2.00 than is obtained experimentally. Thus, the SCF-X α -SW calculations are producing too covalent a description of the active site. There is one set of adjustable parameters in this calculation, which is the sphere sizes used in the scattered wave solutions. Those employed in this initial calculation are the standard spheres normally used that are defined by the Norman criteria (37). We systematically varied these spheres (increasing the metal sphere increases its electron density, lowers its effective nuclear charge, and reduces its interaction with the ligands), and iteratively repeated this g value protocol until the calculated values were in good agreement with experiment (33, 36). This approach provided the experimentally adjusted description of the ground state wave function of the blue copper site that is given in Figure 7A.

These X α calculations provide a description of the ground state of the blue copper site that is highly covalent. The covalency is strongly anisotropic with delocalization predominantly into the $S\pi$ orbital of the thiolate (Figure 7A). We have been able to experimentally test the key features of this ground state using a variety of spectroscopic methods. First, the high covalency can be probed by copper L-edge spectroscopy (38). The electric dipole intensity of the $\text{Cu } 2p \rightarrow \Psi_{\text{HOMO}}$ (HOMO is the highest occupied molecular orbital) transition at 930 eV reflects the $\text{Cu } 2p \rightarrow \text{Cu } 3d$ transition probability and probes the amount of Cu $d_{x^2-y^2}$ character in the ground-state wave function. From Figure 7C, it is ob-

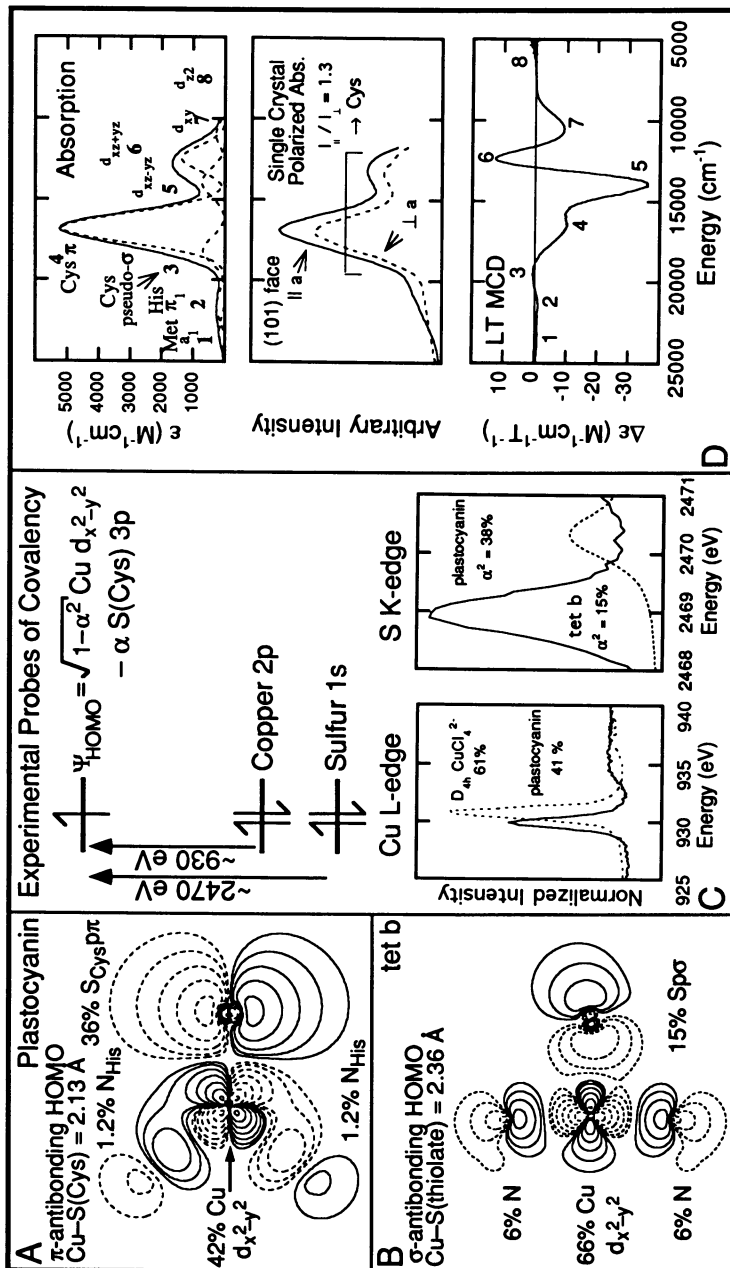


Figure 7. Ground-state wave function of plastocyanin. A: HOMO wave function contour for plastocyanin (28). B: HOMO wave function contour for the thiolate copper complex tet b (34). C: Copper L-edge (38) and sulfur K-edge (34) spectra as probes of metal-ligand covalency. D: Absorption, single-crystal polarized absorption, and low-temperature MCD spectra of plastocyanin. The absorption spectrum has been Gaussian resolved into its component bands as in reference 33.

served that the 930-eV peak in plastocyanin has 67% of the intensity of D_{4h} -CuCl₄²⁻, which is known to have 61% Cu $d_{x^2-y^2}$ character (Figure 1C). Thus, the ground state of the blue copper site is estimated from experiment to have 41% Cu $d_{x^2-y^2}$ character. This is in good agreement with the adjusted SCF-X α -SW calculations (42%). Second, the sulfur contribution to the HOMO can be studied using sulfur K-edge spectroscopy (34) in which the electric dipole intensity now reflects the S1s \rightarrow S3p character in the HOMO. From Figure 7C, plastocyanin exhibits an intense sulfur pre-edge feature at 2469 eV. It has 2.6 times the intensity of the tet *b* model complex of Schugar (39), which contains a normal 2.36 Å copper-thiolate sulfur bond and has 15% sulfur *p* character in the ground state (Figure 7B). Thus, the blue copper site is also experimentally estimated to have 38% sulfur *p* character from the cysteine ligand, again in good agreement with the X α calculations (36%).

The final feature of the ground-state wave function is elucidated through the assignment of the characteristic excited-state absorption spectral features of plastocyanin (Figure 7D). Although there are in fact eight bands required to fit a combination of absorption (Abs), circular dichroism (CD), and magnetic circular dichroism (MCD) spectra of the blue copper site (33), at low resolution the absorption spectrum was regarded originally as having a low-energy weak and higher-energy intense (i.e., the 600 nm, 16,000 cm⁻¹) band pattern (1, 26). Polarized single crystal spectral studies over this region (29) showed the same polarization ratio for both bands, which required that both bands be associated with the Cys S–Cu(II) bond. Thus, in parallel to the Cl⁻ \rightarrow Cu(II) charge-transfer assignment presented earlier, these were assigned as low-energy weak π and higher-energy intense σ charge transfer transitions involving the thiolate sulfur. However, MCD spectroscopy showed that this assignment was not correct. All four of the low-energy bands (5–8 in Figure 7D) that comprise this region are weak in the absorption spectrum but quite intense in the low-temperature MCD spectrum (33). Because MCD C-term intensity for Cu(II) requires spin-orbit coupling, and hence *d* orbital character, this leads to the assignment of bands 5–8 as *d* \rightarrow *d* transitions. Thus, the 600-nm band (4), that is intense in the absorption spectrum and weak in the low-temperature MCD spectrum, is the lowest-energy charge-transfer transition from the thiolate and must be the Cys $p\pi \rightarrow$ Cu $d_{x^2-y^2}$ charge-transfer transition. The Cys $p\sigma \rightarrow$ Cu $d_{x^2-y^2}$ is a weak band at higher energy. The key point is that for the blue copper site one has a low-energy intense π and higher energy weak σ charge-transfer transition to the Cu $d_{x^2-y^2}$ orbital. Inasmuch as charge-transfer intensity reflects orbital overlap, this overlap requires that the $d_{x^2-y^2}$ orbital have its lobes bisected by the Cys S–Cu bond (Figure 7A) and thus be involved in a strong π antibonding inter-

action with the thiolate as also obtained from the $X\alpha$ calculations. The strong π interaction rotates the $d_{x^2-y^2}$ orbital by 45° relative to its usual orientation along the ligand–copper bond as, for example, in the tet *b* model complex (Figure 7B). This rotation of the $d_{x^2-y^2}$ orbital derives from the quite short blue copper Cys S–Cu bond length of 2.13 Å.

Thus the SCF- $X\alpha$ -SW calculations are producing an accurate description of the ground state of the blue copper site and one can now correlate this with crystal structure information to obtain significant insight into function. In particular, the X-ray structure of ascorbate oxidase (40) shows that the cysteine ligand of a blue copper site in this multicopper oxidase is flanked on either side in the sequence by histidines that are ligands to two of the coppers in a trinuclear copper cluster site (discussed in the later section, *Multicopper Oxidases*) (41). This blue copper site transfers an electron rapidly in the reduction of O_2 at the trinuclear copper center. As can be seen from the $X\alpha$ calculated wave function contour that we have superimposed on the crystal structure of the blue center in ascorbate oxidase (Figure 8), the ground-state wave function provides a highly anisotropic covalent pathway involving the cysteine sulfur. The covalency activates this residue for directional electron transfer. In addition, the low-energy, intense Cys $\pi \rightarrow Cu\ d_{x^2-y^2}$ charge-transfer transition in the blue copper absorption spectrum provides an efficient hole superexchange pathway for rapid electron transfer between the blue and trinuclear copper cluster sites (2). Clearly, as shown in Figure 8, the unique electronic structure of the blue copper center reflects a ground-state wave function that plays a critical role in its functioning of rapid long-range electron transfer to a specific location in or on the protein.

Coupled Binuclear Copper Proteins

The binuclear copper proteins hemocyanin and tyrosinase reversibly bind dioxygen and in the case of tyrosinase activate it for hydroxylation of phenol to *ortho*-diphenol and further oxidation to *ortho*-quinone (Figure 9) (42). Both proteins have essentially the same oxy active sites (42, 43) that involve two Cu(II) ions (shown by X-ray absorption edge data (44, 45)) and bound peroxide (shown by the unusually low O–O stretching frequency of 750 cm⁻¹ observed in the resonance Raman spectrum (46–48)). As will be summarized in this section, the unique vibrational and ground and excited state electronic spectral features of this oxy site are now understood. These generate a detailed description of the peroxide–copper bond that provides fundamental insight into the reversible binding and activation of dioxygen by this site.

The ground state of oxyhemocyanin exhibits no EPR signal. This results from a strong antiferromagnetic coupling of the two Cu(II) ions

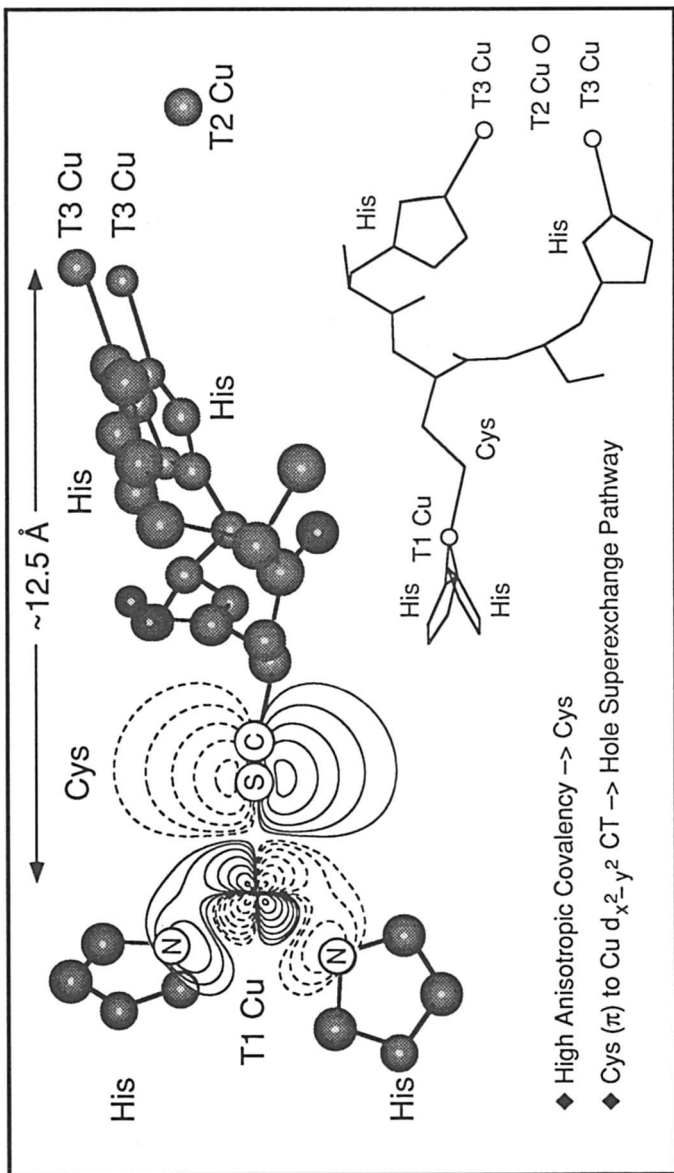
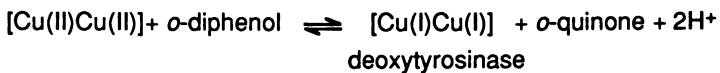
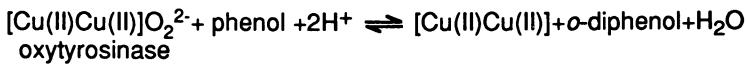
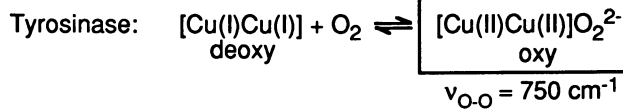
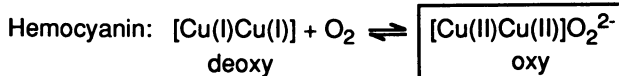


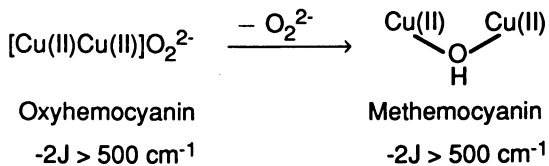
Figure 8. Proposed electron transfer pathway in blue copper proteins. The plastoxygen wave function contours have been superimposed on the blue copper (type I) site in ascorbate oxidase (40). The contour shows the substantial electron delocalization onto the cysteine $S\pi$ orbital that activates electron transfer to the trinuclear copper cluster at 12.5 Å from the blue copper site. This low-energy, intense Cys Sp → Cu charge-transfer transition provides an effective hole superexchange mechanism for rapid long-range electron transfer between these sites (2, 3, 28).

Reactivity



Ground State

No EPR → Antiferromagnetic coupling ($\mathcal{H} = -2J \mathbf{S}_1 \cdot \mathbf{S}_2$)



Excited States

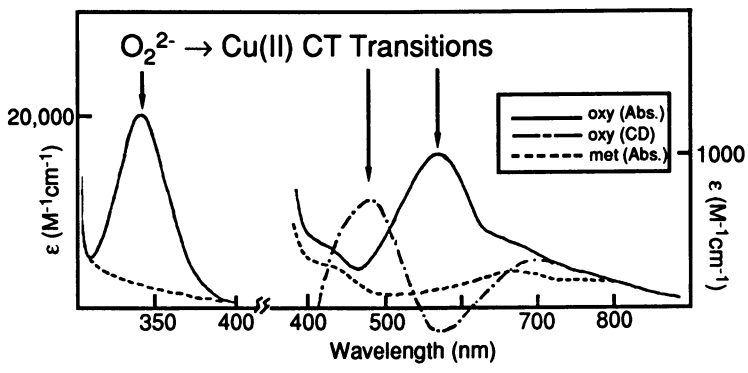


Figure 9. Coupled binuclear copper proteins; ground- and excited-state spectral features.

($-2J > 500 \text{ cm}^{-1}$), (49, 50) hence its classification as a *coupled* binuclear copper site (51). Displacement of the peroxide produces a met derivative that also has two Cu(II) ions that are strongly antiferromagnetically coupled ($-2J > 500 \text{ cm}^{-1}$) (Wilcox, D. E.; Westmoreland, T. D.; Sandusky, P. O.; Solomon, E. I., unpublished results). Thus, there must be an endogenous bridge present in the met derivative. The crystal structure of deoxyhemocyanin (52) shows no protein residues capable of bridging the copper ions in the vicinity of the binuclear copper site so this bridging ligand is likely to be hydroxide. With respect to the excited state spectroscopy, oxyhemocyanin exhibits a moderately intense band in the absorption spectrum at $\sim 600 \text{ nm}$ ($\epsilon \sim 1000 \text{ M}^{-1} \text{ cm}^{-1}$) and an extremely intense band at $\sim 350 \text{ nm}$ ($\epsilon \sim 20,000 \text{ M}^{-1} \text{ cm}^{-1}$). Displacement of peroxide on going to the met derivative (solid to dashed spectrum in Figure 9, bottom) eliminates these features as well as a band at 480 nm that is present in the CD but not the absorption spectrum (53). These three bands can be assigned as peroxide-to-copper charge transfer transitions and will be seen to provide a detailed probe of the peroxide–copper bond. We are particularly interested in (1) the fact that there are three charge transfer bands, (2) the selection rules associated with the presence of a band in the CD but not absorption spectrum, and (3) the high energy and intensity of the 350-nm band.

We first consider peroxide bound end-on to a single Cu (II) ion (Figure 10A). The valence orbitals of peroxide involved in bonding are the π^* set. These orbitals split into two nondegenerate levels (labeled π_{σ}^* and π_{ν}^*) on bonding to the metal ion. The π_{σ}^* orbital is oriented along the Cu–O bond and has strong overlap with the $d_{x^2-y^2}$ orbital producing a higher-energy, intense charge-transfer transition. The peroxide π_{ν}^* orbital is vertical to the Cu–O bond and weakly π interacting with the copper, producing a lower-energy, relatively weak transition. Thus, end-on peroxide bonding is dominated by the σ donor interaction of the $\text{O}_2^{2-} \pi_{\sigma}^*$ orbital with the $d_{x^2-y^2}$ orbital. This predicted low-energy weak/high-energy intense charge-transfer spectrum is observed experimentally for the $[\text{Cu}_2(\text{XYL-O})(\text{O}_2)]^+$ complex prepared by Karlin (54) that has O_2^{2-} end-on bound to a single Cu(II) ion (based on mixed isotope effects on its resonance Raman spectrum) (Figure 10B) (55). Note, however, that there are only two bands in the charge–transfer spectrum of this monomeric complex and that the π_{σ}^* transition is considerably lower in energy (500 nm) and weaker in intensity ($\epsilon \sim 5000 \text{ M}^{-1} \text{ cm}^{-1}$) than the 350 nm O_2^{2-} charge-transfer band in oxyhemocyanin.

The fact that three peroxide-to-copper charge–transfer transitions are observed in oxyhemocyanin and oxytyrosinase led us to consider the spectral effects of bridging peroxide between two Cu(II) ions. A transition-dipole vector-coupling (TDVC) model was developed that predicts that each charge-transfer state in a Cu–peroxide monomer

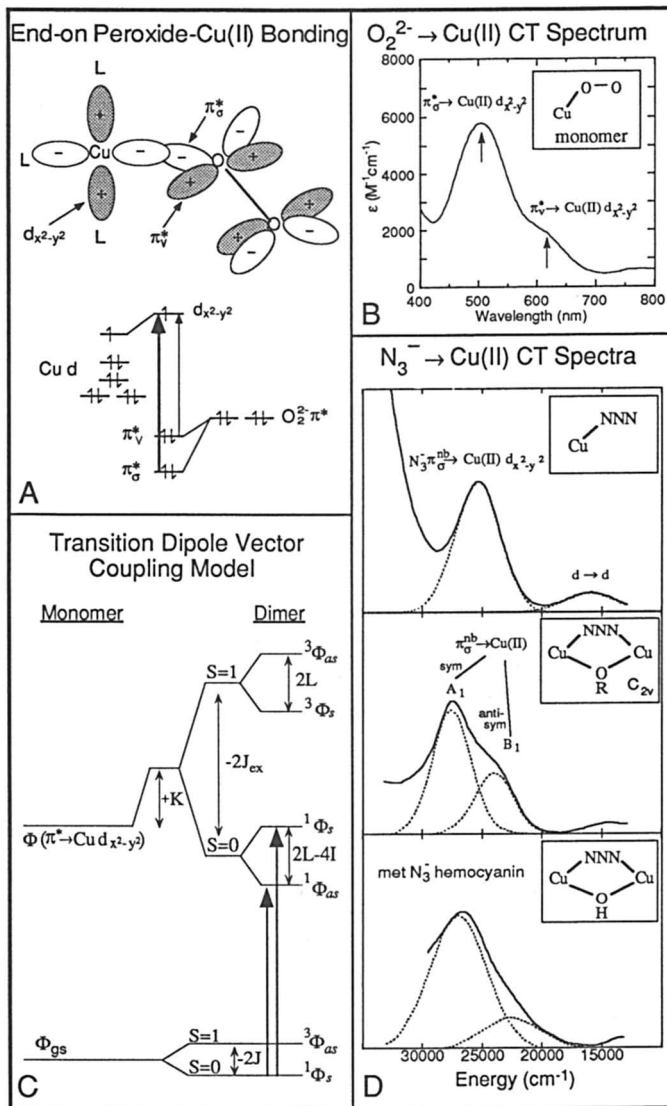


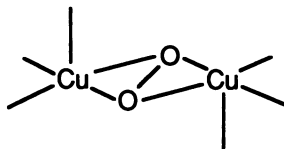
Figure 10. Peroxide charge-transfer transitions in copper monomers and dimers. A: Orbital interactions involved in end-on peroxide–copper bonding and predicted charge-transfer transitions (thickness of arrow indicates relative intensity). B: Charge-transfer absorption spectrum of peroxide bound to a single Cu(II) ion (Adapted from ref. 55). C: Ground-state and charge-transfer excited state splittings due to dimer interactions in a peroxide bridged copper dimer. K is the coulomb dimer interaction, J_{ex} is the excited-state magnetic exchange, and I and L are the coulomb and exchange contributions to the excitation transfer between halves of the dimer, respectively. D: Azide-to-copper charge-transfer spectra of model complexes and met azide hemocyanin (Adapted from ref. 56).

complex will split into four states in a dimer (Figure 10C) (53, 56–58). We have further developed a general model of excited state dimer interactions, the valence bond-configurational interaction (VBCI) model. This model reduces to the TDVC model in the in-state limit but the VBCI treatment gives a quantitative description of the dimer splittings in terms of parameters that can be evaluated using SCF-X α molecular orbital calculations (58–60). First, there is a singlet–triplet antiferromagnetic splitting in the excited state just as there is in the ground state but considerably larger in magnitude (58). In addition, both the singlet and triplet states are split further into two states that correspond to symmetric and antisymmetric combinations of the O₂²⁻ → Cu(II) charge-transfer transition to each copper in the bridged dimer. As the antiferromagnetically coupled ground state is a singlet, only the two transitions to the singlet excited states should have absorption intensity. This predicted splitting into two bands is observed (56) in a series of azide model complexes prepared by Sorrell (61), Reed (62, 63), and Karlin (64) (Figure 10D). Azide bound to a single Cu(II) ion exhibits a π_σ^{nb} → Cu(II) charge-transfer transition that is analogous to the peroxide π_σ* → Cu(II) charge-transfer transition. As predicted, bridging the azide in a *cis* μ-1,3 geometry between two Cu(II) ions results in a splitting of the monomer charge-transfer transition into two bands, the symmetric (A1 in the C_{2v} dimer symmetry) and antisymmetric (B1) components of the π_σ* charge-transfer transition. Note in Figure 10D (bottom) that binding N₃⁻ to the met hemocyanin derivative produces the same A1/B1 charge-transfer intensity pattern indicating that azide also bridges in a *cis* μ-1,3 geometry in met hemocyanin (56).

The preceding discussion shows that the presence of more than two peroxide-to-copper CT transitions in oxyHc requires that this ligand bridge the copper centers. In 1989, Kitajima obtained the first crystal structure of a side-on bridging peroxide in transition-metal chemistry (65, 66) and, in 1992, Magnus determined that *Limulus polyphemus* oxyHc has the side-on bridging structure shown in Figure 11 (top) (67). The VBCI model can then be used to predict the energy splittings and symmetries and hence the selection rules for the peroxide-to-copper CT transitions in the effective D_{2h} symmetry of the side-on bridged site (the *trans* axial His ligands reduce the site symmetry to C_{2h} but have a small effect on the spectrum) (59, 60). Bridging the peroxide in the side-on structure results in a splitting of the π_v* into two components. The low-energy component is electric dipole allowed (z) and should appear in the absorption spectrum, but with limited intensity inasmuch as it is a π_v* charge-transfer transition. This can be associated with the 600-nm absorption band. The second component of the peroxide π_v* charge-transfer transition is predicted to be only magnetic dipole allowed (R_y) and thus it should contribute to the CD but not absorption spectrum.

Oxyhemocyanin and Oxytyrosinase

Limulus Oxyhemocyanin X-ray Crystal Structure



K. Magnus, H. Ton-That
J. Inorg. Biochem.
47, 20 (1992)

Side-on $\mu\text{-}\eta^2:\eta^2$ Bridge

Excited State Spectral Assignments

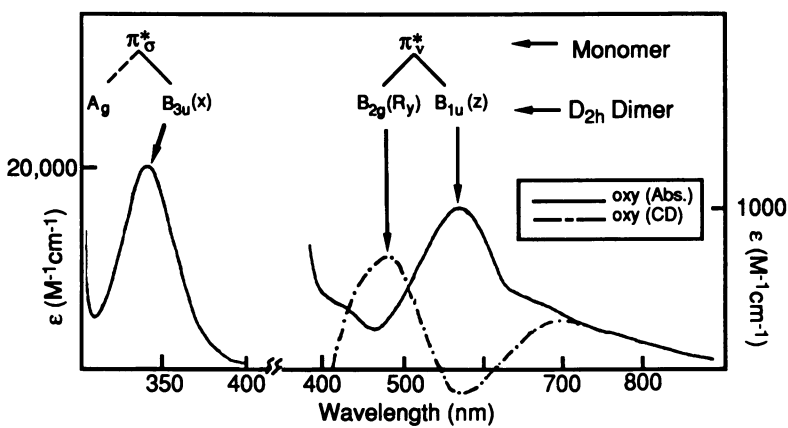
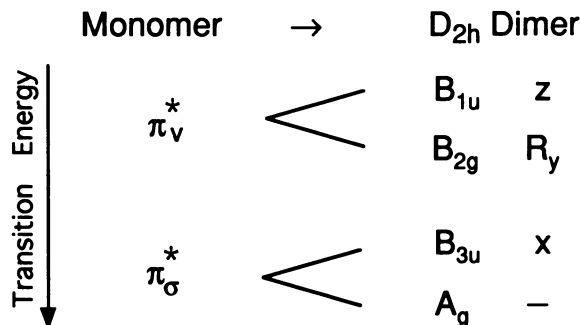


Figure 11. Excited-state spectral assignments for the D_{2h} $\mu\text{-}\eta^2:\eta^2$ peroxo-copper unit in oxyhemocyanin and oxytyrosinase.

The 480-nm CD feature can be assigned to this transition. The π_{σ}^* also splits into two bands with the lower-energy component being electric dipole allowed and having the dominant absorption intensity. This can be associated with the 350-nm absorption band in oxyhemocyanin. Thus, the side-on bridging peroxide produces the three observed charge-transfer transitions with one being present in the CD but not the absorption spectrum. However, one must still account for the high intensity and energy of the 350-nm O_2^{2-} π_{σ}^* charge-transfer transition and the low vibrational frequency of the O–O stretch. Thus we proceed to evaluate quantitatively the electronic structure associated with the side-on bridging peroxide and compare this to the more commonly observed end-on bridging peroxide structure both theoretically and experimentally.

Broken-symmetry, spin-unrestricted SCF-X α -SW MO calculations were performed to describe the electronic structures associated with both the end-on and side-on bridging peroxide geometric structures (68, 69). These calculations are appropriate for antiferromagnetically coupled dimers (70, 71). In Figure 12, we focus on the interaction of the highest occupied molecular orbital (HOMO) and the lowest unoccupied molecular orbital (LUMO), that are the symmetric and antisymmetric combinations of $d_{x^2-y^2}$ orbitals on each copper, with the valence orbitals of the peroxide. For the end-on bridged structure (Figure 12, left), the bonding is consistent with the qualitative description presented earlier. The peroxide π_{σ}^* orbital is stabilized through a bonding interaction with the LUMO on both coppers. Thus, in the end-on bridged geometry peroxide acts as a σ donor ligand with one bonding interaction with each of the two coppers. A very different bonding description is obtained for the side-on bridged peroxide. In this structure, the π_{σ}^* orbital is again stabilized by a σ donor interaction with the LUMO on both coppers. In the side-on structure the bonding/antibonding interaction of the π_{σ}^* orbital is larger than in the end-on structure because the peroxide now occupies two coordination positions on each of the two coppers. Thus, peroxide behaves as an extremely strong σ donor in the side-on structure. Furthermore, the side-on peroxide is predicted to have an additional bonding interaction with the $d_{x^2-y^2}$ orbitals on the coppers. This involves stabilization of the HOMO through its interaction with the high-energy unoccupied σ^* orbital on the peroxide. This additional bonding interaction shifts electron density from the copper ions onto the peroxide. Thus, peroxide also acts as a π acceptor ligand using this highly antibonding σ^* orbital.

It was of critical importance to evaluate experimentally this unusual electronic structure description for the side-on bridged peroxide and its relation to the spectral features of the $\mu\text{-}\eta^2\text{:}\eta^2$ model complex and oxyhemocyanin. This evaluation was accomplished through a series of

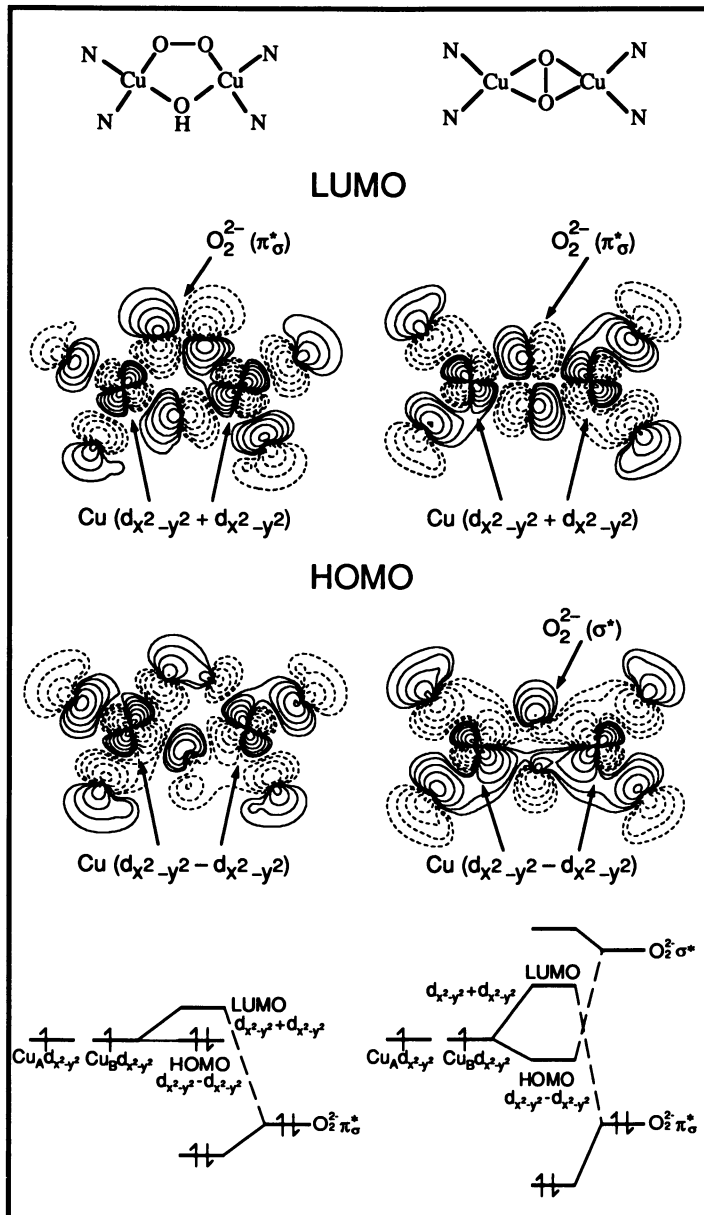


Figure 12. Electronic structures of the end-on cis- μ -1,2 (C_{2v}) and side-on $\mu\text{-}\eta^2:\eta^2$ (D_{2h}) models of the oxyhemocyanin active site. Wave function contours of the HOMO and LUMO and energy level diagrams showing dominant orbital contributions.

studies of the charge-transfer and vibrational spectral features of end-on (72) and side-on (73) bound peroxide–copper model complexes prepared by Karlin (74) and Kitajima (65, 66). The σ -donor ability of peroxide can be related to the intensity (and energy (58)) of the $\pi_{\sigma}^* \rightarrow \text{Cu(II)}$ charge-transfer transition (Figure 13). The idea is that as the wave function of the occupied $\text{O}_2^{2-} \pi_{\sigma}^*$ orbital gains copper character, α (i.e., the coefficient for the amount of copper character in the wave function is α), its σ -donor interaction with the copper increases. This wave function gives an approximation for the ligand-to-metal charge-transfer intensity that (along with geometric factors) is proportional to α^2 . Thus, the peroxide $\pi_{\sigma}^* \rightarrow \text{Cu(II)}$ charge-transfer intensity increases as its σ -donor interaction with the copper increases. If we normalize to the π_{σ}^* charge-transfer intensity of the end-on peroxide monomer complex shown in Figure 10B, the O_2^{2-} charge-transfer intensity of the *trans* μ -1,2 end-on bridged complex increases by a factor of two, consistent with peroxide binding to each of two Cu(II) ions. Although no *cis* model complex exists, our $\text{X}\alpha$ calculations indicate that peroxide binding in this geometry should have a similar σ -donor interaction with the coppers as peroxide bridged in the *trans* complex. However, the side-on bridged $\mu\text{-}\eta^2:\eta^2$ complex and oxyhemocyanin exhibit an extremely intense π_{σ}^* charge-transfer transition. The intensity of this transition quantitates to ~ 4 times the σ -donor interaction of peroxide bound to a single Cu(II) ion. This is consistent with the $\text{X}\alpha$ calculations and the fact that in this geometry peroxide has four bonding interactions with the two Cu(II) ions. The extremely high intensity of the 350-nm band in oxyhemocyanin also quantitates to having ~ 4 σ -donor interactions with the binuclear copper site consistent with the side-on peroxide bridged structure of oxyhemocyanin.

One can probe the π -acceptor ability of the peroxide through a study of its intraligand stretching force constant (and hence O–O bond strength), which is obtained from a normal coordinate analysis (NCA) of vibrational spectra (Figure 13). One would expect this force constant to increase as the σ -donor interaction of the peroxide with the copper increases, because this increased interaction removes the electron density from a π -antibonding orbital on the peroxide that increases its intraligand bond strength. This increase in bond strength is observed experimentally by comparing the end-on monomer to the *trans* end-on dimer, in which the O–O vibrational frequency increases from 803 to 832 cm^{-1} . This increase in vibrational frequency is consistent with the *trans* end-on dimer having σ -donor interactions with two coppers (72). However, on going to the side-on peroxy bridging geometry, the O–O stretching frequency dramatically decreases in the $\mu\text{-}\eta^2:\eta^2$ model complex and oxyhemocyanin, yet in this geometry the peroxide is the strongest σ donor, based on the high charge-transfer intensity associated with four

σ-Donor Ability: $O_2^{2-} \rightarrow Cu$ charge transfer transition intensity (and energy)

$$\Psi_{\sigma}^* = (1-\alpha^2)^{1/2} \pi_{\sigma}^* - \alpha d_{x^2-y^2}$$

$$I_T \propto \alpha^2 (1-\alpha^2) (r \cos \phi)^2$$

	π-Acceptor Ability: ν_{O-O} ($+\nu_{M-L}$) $\xrightarrow{NCA} k_{O-O}$	π-Acceptor Ability: ν_{O-O} ($+\nu_{M-L}$) $\xrightarrow{NCA} k_{O-O}$
k_{O-O} increases for σ-donor ($O_2^{2-} \cdot \pi^*$)		
k_{O-O} decreases for π-acceptor ($O_2^{2-} \cdot \sigma^*$)		
	K. Karlin	N. Kitajima
σ-donor: relative α^2 (osc. str.)	1 (0.105)	1.9 (0.252)
		3.7 (0.479)
π-acceptor: $k_{O-O}/\text{mdyne/cm}^2$ (ν_{O-O})	2.9 (803)	3.1 (832)
		2.4 (763) <i>i</i> -Pr (749)
		3.7 (0.488) (750)
		<i>L. Polyphemus</i>

Figure 13. Electronic structures of end-on and side-on peroxide bridged models of oxyhemocyanin. Comparison of experimentally determined peroxide σ-donor and π-acceptor abilities.

bonding interactions to the two Cu(II) ions. Although the mechanical coupling of the vibrations in this geometry is complicated, a normal coordinate analysis on the side-on bridged model complex gives a significantly lower O–O force constant indicating an extremely weak O–O bond (73). This is experimental evidence confirming the Xα calculated prediction that side-on bridged peroxide also participates in a π-acceptor interaction with the coppers that shifts some electron density into the strongly antibonding σ* orbital on the peroxide.

With the novel electronic structure of the side-on bridged peroxy-binuclear cupric site of oxyhemocyanin and oxytyrosinase having been determined, it is now possible to evaluate electronic structure contributions to the functions of these protein active sites (68, 69) (Figure 14). The combination of strong σ-donor and π-acceptor interactions with the coppers leads to a very strong dioxygen–copper bond in the side-on structure that would contribute to reversible O₂ binding and, in particular, stabilize the bound peroxide with respect to decay to the inactive met site in hemocyanin. These bonding interactions further provide a major electronic structure contribution to the mechanism of dioxygen activation in oxytyrosinase. The strong σ-donor interaction with the coppers results in a less negative peroxide, promoting electrophilic attack on substrate while the π acceptor contribution to the bonding shifts a small amount of electron density into the peroxide σ* orbital that leads to an extremely weak O–O bond activating it for cleavage. As shown in Figure 14, we found that a major difference between hemocyanin and tyrosinase is that the phenolic substrate can access and bind to the Cu center in tyrosinase. The substrate then contributes electron density into the LUMO, which is antibonding with respect to both the O–O and Cu–O bonds, and thus further initiates oxygen transfer in catalysis.

Multicopper Oxidases

The final section of this chapter focuses on the multicopper oxidases. The multicopper oxidases use at least four copper ions, which are grouped into three types based on their spectral properties, to couple four one-electron oxidations of substrate to the four-electron reduction of dioxygen to water (Figure 15). Two of the coppers form an antiferromagnetically coupled pair that is referred to as a type 3 center. The type 1 center is a blue copper site as discussed earlier, and the type 2 copper is “normal” in the sense of having a tetragonal Cu(II) EPR spectrum ($g_{\parallel} > g_{\perp} > 2.00$, $A_{\parallel} > 140 \times 10^{-4} \text{ cm}^{-1}$) and weak ligand field absorption features in the visible spectrum (75) as discussed earlier for normal copper complexes. Laccase is the simplest of the multicopper oxidases and contains one of each type of center for a total of four copper ions in the native enzyme (1, 2, 76–80). Understanding the reactivity of

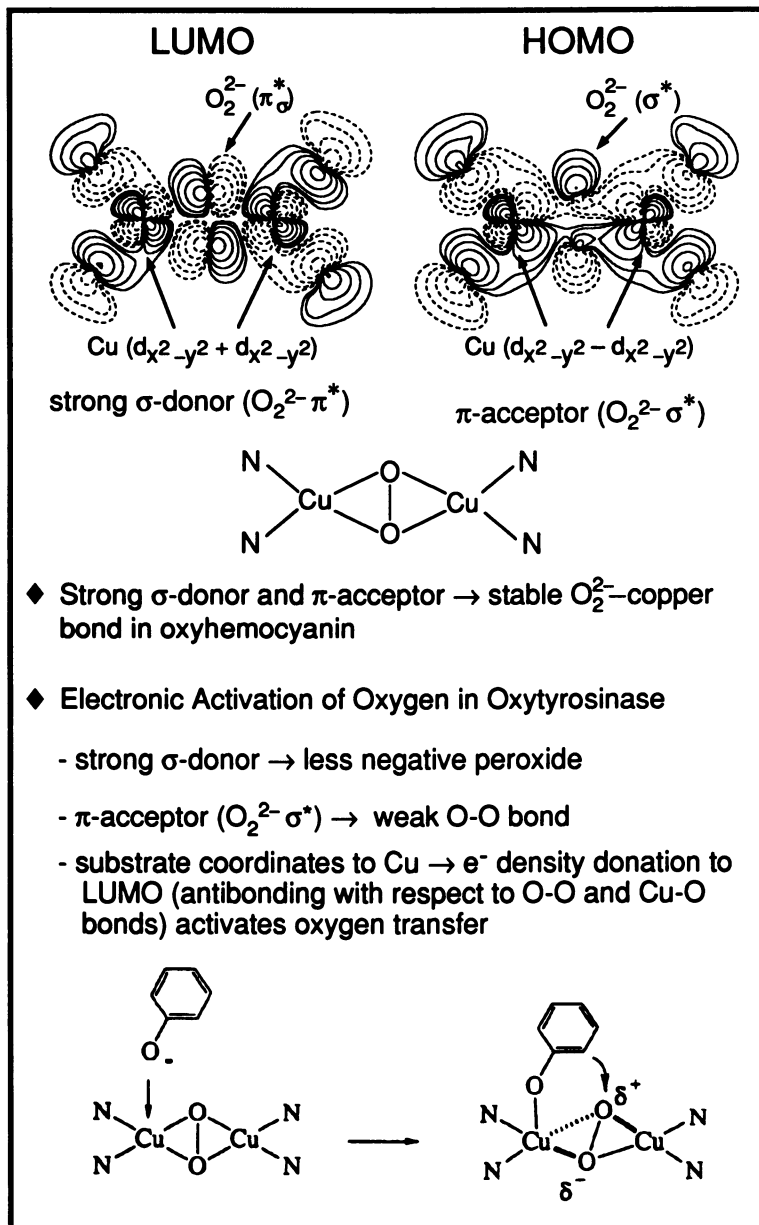


Figure 14. Electronic structural contributions to oxygen binding and activation in hemocyanin and tyrosinase.

<u>Reactivity</u>				
$4\text{AH} + \text{O}_2 \longrightarrow 4\text{A} + 2\text{H}_2\text{O}$				
<u>Number of Centers</u>				
Multicopper Oxidases:	Type 1 (Blue)	Type 2 (Normal)	Type 3 (Coupled Binuclear)	Total Cu
Laccase	1	1	1	4
Ascorbate Oxidase	2	2	2	8
Ceruloplasmin	2	1	1 or 2	5 - 7
Laccase Derivatives:				
Type 2 Depleted (T2D)	1	--	1	3
Type 1 Hg Sub. (T1Hg)	Hg ²⁺	1	1	3

Figure 15. Multicopper oxidases: reactivity and stoichiometry.

this enzyme is a complex problem, and two derivatives have served to simplify this system. In type 2 depleted (T2D) laccase, the type 2 copper is reversibly removed leaving the type 1 and type 3 centers (81). The type 1 mercury substituted derivative (T1Hg) is formed by replacing the type 1 copper with the spectroscopic and redox innocent mercuric ion (82).

The goal of our research on the multicopper oxidases has been to determine the spectral features of the type 3 (and type 2) centers, to use these spectral features to define geometric and electronic structural differences relative to hemocyanin and tyrosinase, and to understand how these structural differences contribute to their variation in biological function. The hemocyanins and tyrosinases reversibly bind and activate dioxygen whereas the multicopper oxidases catalyze its four-electron reduction to water.

We start by defining the spectral features associated with each type of copper in native and T2D laccase (Figure 16). The EPR spectrum of the native enzyme contains contributions from two distinct cupric sites (Figure 16A); one with a large and a second with a small parallel hyperfine splitting. These have been assigned to the type 2 and type 1 copper sites, respectively. The EPR spectrum of the T2D derivative contains a single component, with a small hyperfine coupling, that is assigned to the type 1 copper center (83). The type 3 copper atoms are EPR nondetectable and, by analogy to hemocyanin and tyrosinase, can

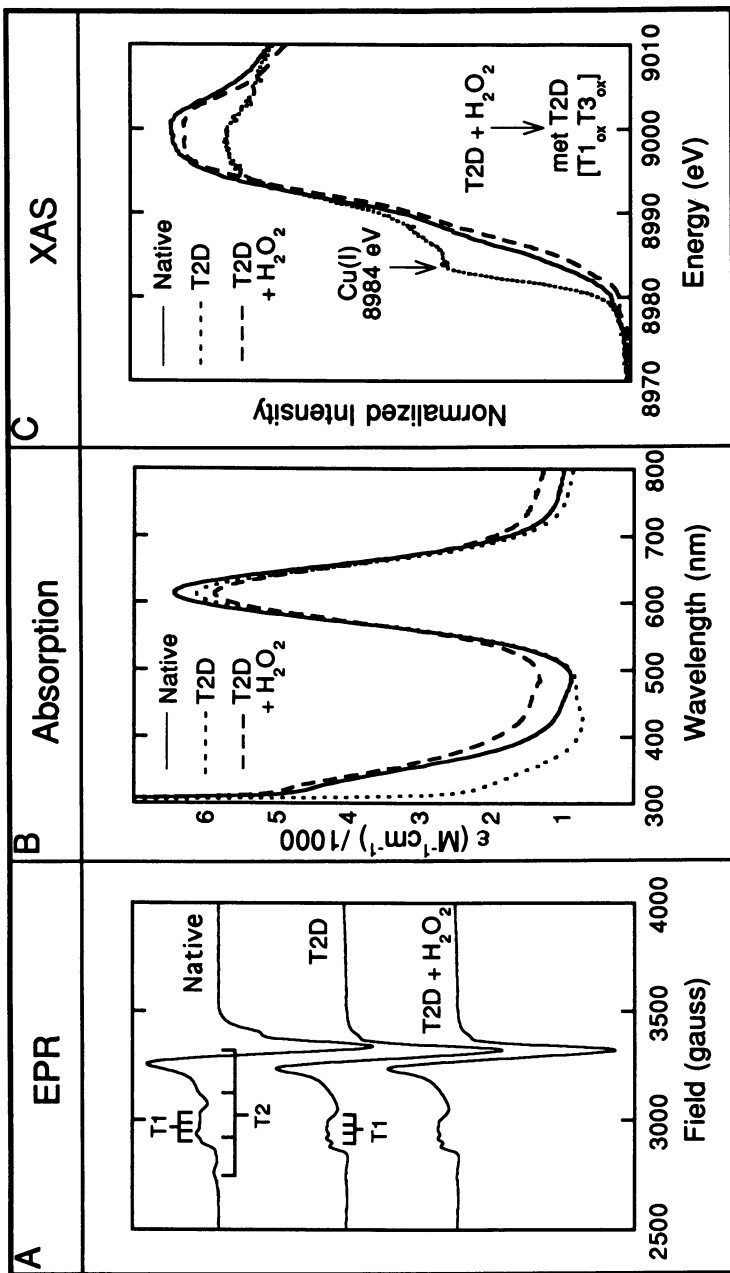


Figure 16. Spectral features of native and T2D laccase. A: EPR. B: Visible absorption. C: X-ray absorption spectra of native, T2D, and T2D laccase following reaction with hydrogen peroxide.

be considered to be a coupled binuclear copper site. The absorption spectrum of native and T2D laccase (Figure 16B) exhibits an intense thiolate S → Cu(II) charge-transfer transition at 600 nm, which is assigned to the type 1 copper center (4). The only spectral feature that has been associated with the type 3 center is the absorption band centered at 330 nm ($\epsilon \sim 3000 \text{ M}^{-1} \text{ cm}^{-1}$). This band decreases in intensity with reduction of the protein by two electrons (at the same potential). The 330-nm spectral region is expected to contain histidine and hydroxide-to-type 3 Cu(II) charge-transfer transitions (84).

The assignment of the 330-nm absorption band in native laccase to the type 3 center, however, was complicated by the absence of a 330-nm band in the absorption spectrum of T2D laccase (which still contains a type 3 site) (Figure 16B). We discovered a key reaction that clarified the assignment of the 330-nm absorption band. Addition of peroxide to T2D laccase leads to the reappearance of the 330-nm band (85). This indicates that the type 3 site in T2D laccase was reduced (even when exposed to dioxygen) but that the stronger oxidant, peroxide, was capable of oxidizing the type 3 center. This finding was confirmed using X-ray absorption studies at the Cu K-edge (9000 eV) (86). The T2D derivative exhibits a peak at 8984 eV (Figure 16C) that is characteristic of Cu(I) in a three-coordinate site. The magnitude of the 8984-eV band could be quantitated using a normalized edge method that we have developed. We determined that the T2D derivative contained a fully reduced type 3 site. Addition of peroxide eliminated the 8984-eV peak, which indicates that peroxide fully oxidizes the type 3 center to form a met T3 site.

Having defined the T2D derivative, we could study the type 3 site in the absence of the type 2 copper and compare it to the coupled binuclear site in hemocyanin and tyrosinase (Figures 17 and 18). First, as demonstrated from the X-ray edges in Figure 16C, the fully reduced type 3 site is strikingly different from that of hemocyanin and tyrosinase inasmuch as it does not react with dioxygen (85, 86). Peroxide does oxidize the site, and we can further compare this met type 3 center in laccase to met hemocyanin. As with hemocyanin, the met type 3 site in the multicopper oxidases is strongly antiferromagnetically coupled (49, 50, 75). This indicates the presence of an endogenous hydroxide bridge, which has been confirmed by X-ray crystallography (87).

One-electron reduction of met derivatives of hemocyanin and T2D laccase produces the mixed-valent half-met sites that exhibit dramatic differences (Figure 18). In particular, half-met hemocyanin has very unusual coordination chemistry with respect to exogenous ligand binding. For example, azide binds to this half-met active site with an equilibrium binding constant that is more than two orders of magnitude greater than that of azide binding to aqueous Cu(II), and this binding

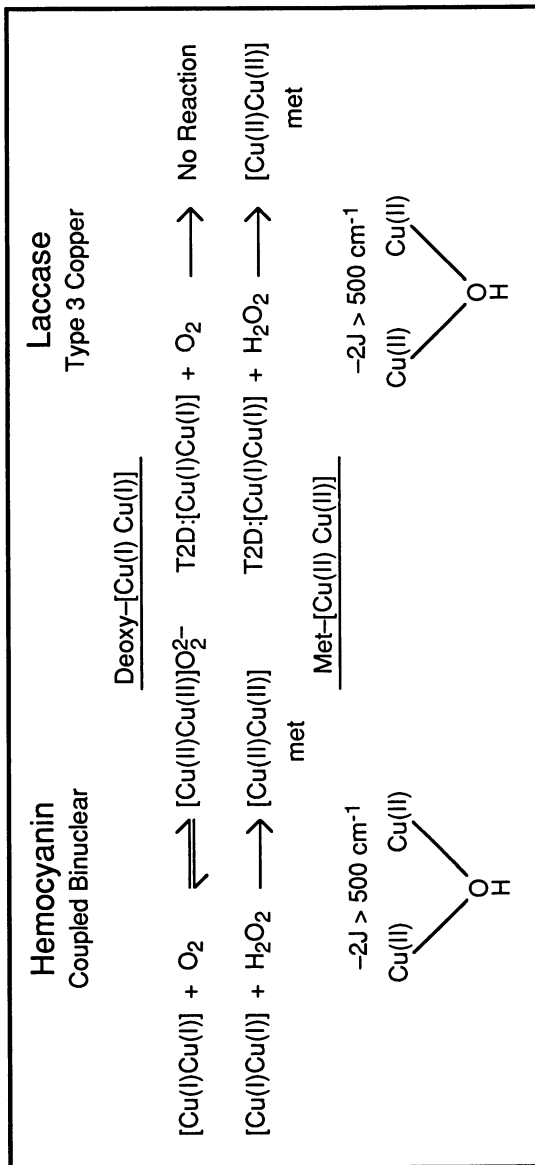


Figure 17. Comparison of the reactivity and magnetism of deoxy and met hemocyanin and the laccase type 3 copper site in the T2D derivative.

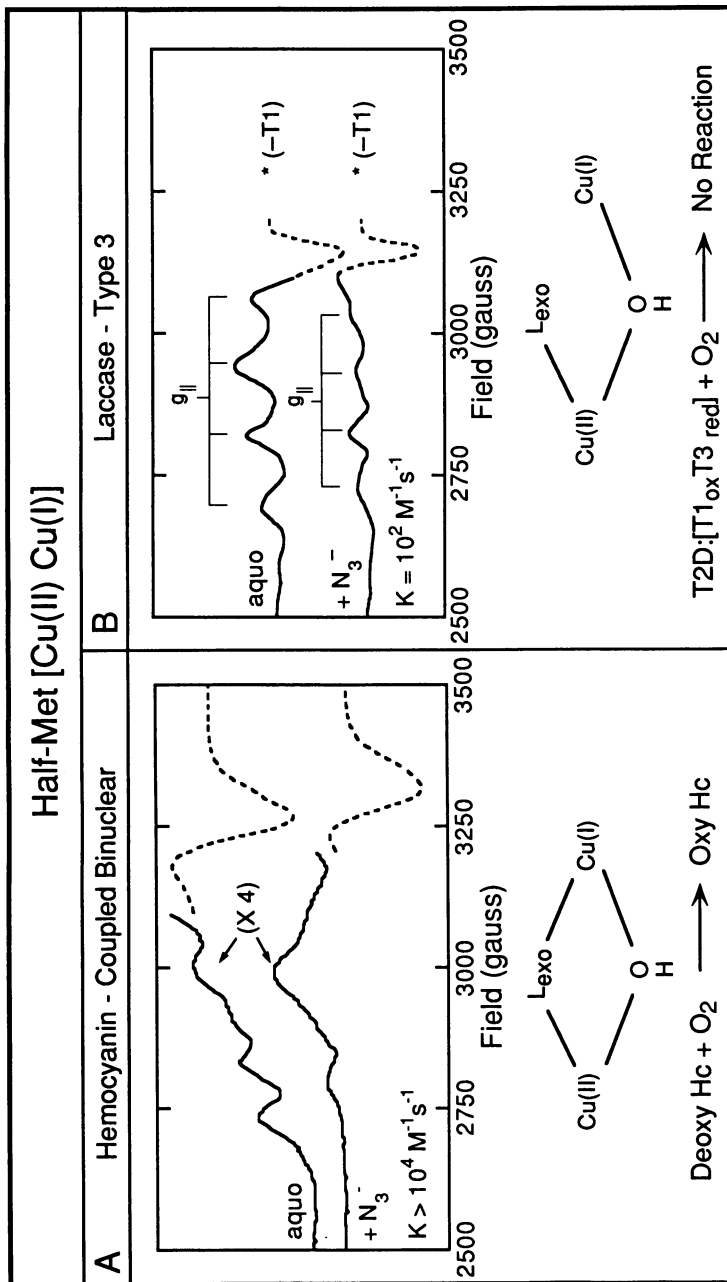


Figure 18. Comparison of half-met hemocyanin with the half-met type 3 (in T2D) laccase copper sites. A: EPR spectra and binding constants of exogenous azide binding. B: Spectroscopically effective structural models for exogenous ligand binding to the half-met derivatives and their relation to differences in dioxygen reactivity.

results in quite unusual mixed-valent spectral features (88). We have studied this unusual half-met hemocyanin chemistry and spectroscopy in some detail (88) and determined that these derive from the fact that exogenous ligands bridge between the Cu(II) and Cu(I) of this mixed-valent site (Figure 18A, bottom). Alternatively, the half-met type 3 site in T2D laccase exhibits normal Cu(II) EPR spectra for all exogenous ligand-bound forms and has an equilibrium binding constant consistent with aqueous Cu(II) chemistry, indicating that the exogenous ligands bind terminally to the Cu(II) of the half-met type 3 site (84). This difference in exogenous ligand binding modes (bridging vs. terminal) directly correlates with differences in O₂ reactivity of these binuclear copper sites as described above in that only the deoxyhemocyanin site reversibly binds dioxygen (Figure 18A).

The combination of the type 3 with the type 2 center does, of course, react with dioxygen in the native enzyme. This reaction led us to consider exogenous ligand interactions with both the type 3 and type 2 coppers in native laccase. An appropriate spectral method to study the interaction of exogenous ligands with each center is low-temperature MCD spectroscopy, which allows correlation of excited-state features with ground-state properties (89–91). In particular, the paramagnetic type 2 copper exhibits very different low-temperature MCD features relative to the antiferromagnetically coupled type 3 center (Figure 19). For the type 2 center, both the ground and excited states have S = 1/2 and split in a magnetic field. The selection rules for MCD spectroscopy predict that there should be two transitions to a given excited state that are of equal magnitude but of opposite sign. As the Zeeman splitting will be on the order of 10 cm⁻¹ and absorption bands are on the order of a few thousand cm⁻¹ broad, the positive and negative bands will mostly cancel and produce a broad, weak, derivative-shaped MCD signal known as an A-term. This is observed if both components of the ground state are equally populated. However, as one lowers the temperature the Boltzmann population of the higher-energy component is reduced, cancellation no longer occurs, and one observes intense, low-temperature MCD signals known as C-terms. These can be two to three orders of magnitude more intense than the high-temperature MCD signals.

For the type 3 center, the antiferromagnetic coupling leads to an S = 0 ground state that cannot split in a magnetic field. Thus, this site does not exhibit C-term intensity and the low-temperature MCD spectrum of native laccase will be dominated by the intense C-terms associated with paramagnetic copper centers (89, 90).

Low-temperature MCD spectroscopy was used to probe the effects of binding the exogenous ligand azide to native laccase (89, 90). Titration of the native enzyme with azide produces two N₃⁻ → Cu(II) charge-transfer transitions: one at 500 nm and a second more intense band at

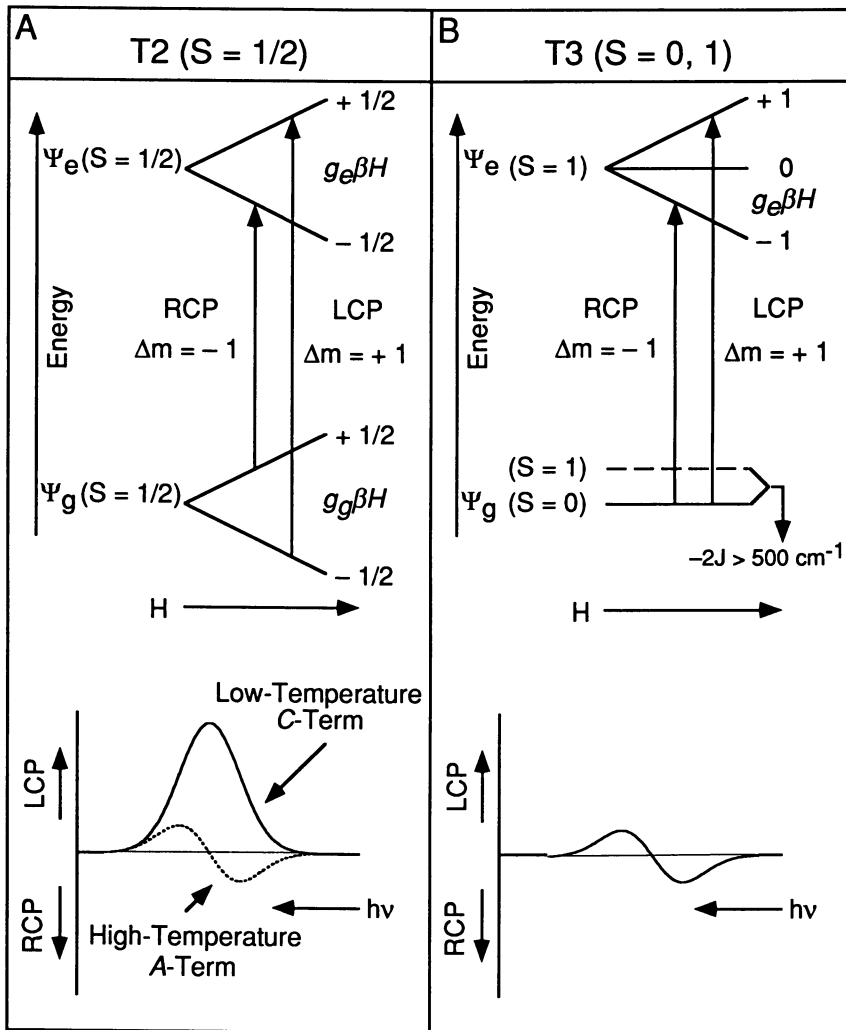


Figure 19. Model for the temperature dependence of the MCD bands of native laccase. A: Transitions and band profiles associated with type 2 copper. B: Transitions and band profiles associated with type 3 copper. Note the difference in temperature dependence of the MCD signal as described in the text.

400 nm (Figure 20A). The intensity of the 400-nm band as a function of azide concentration is plotted as a dashed line in Figure 20C. One can use low-temperature MCD to correlate these excited-state features to specific copper centers. The 500-nm absorption band has a negative low-temperature MCD signal associated with it at 485 nm that increases in magnitude with increasing azide concentration (Figure 20B). The

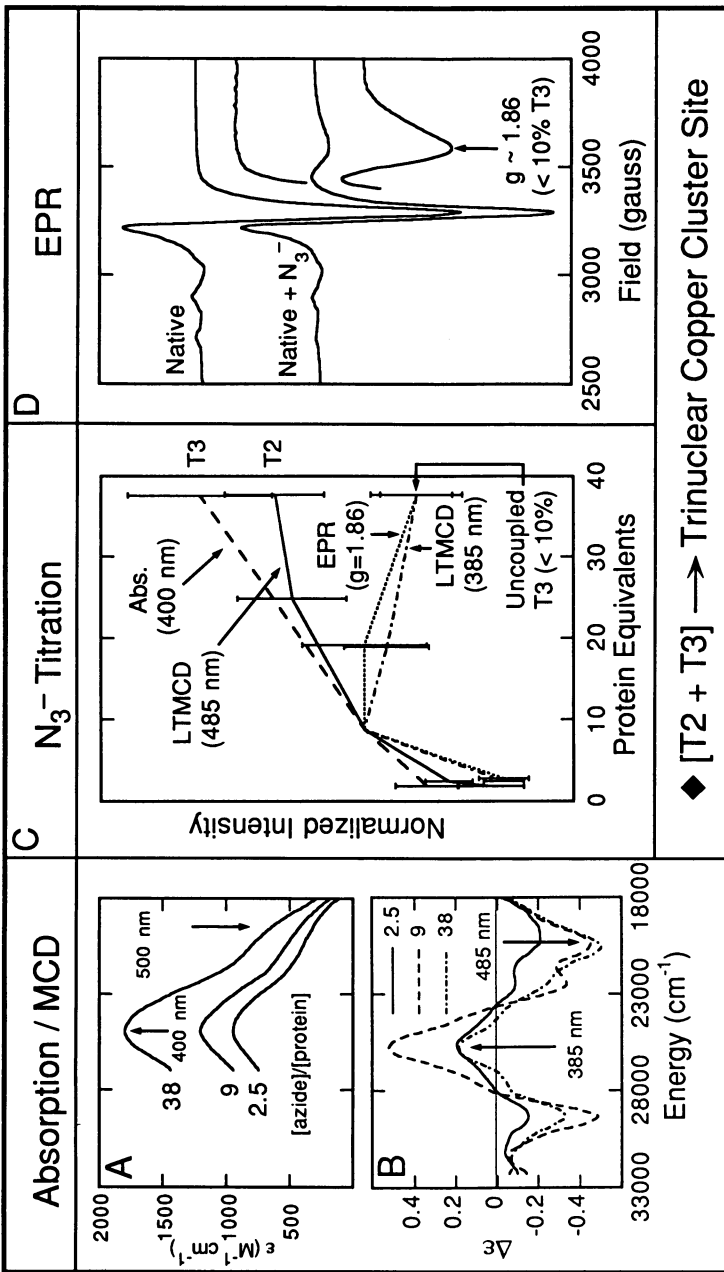


Figure 20. Azide binding to native laccase. A: Difference electronic absorption spectra at 298 K (see reference 89). B: Difference MCD spectra at 4.9 K (5 T). C: Changes in EPR, LTMCD, and absorption intensities plotted as a function of increasing azide concentration. D: EPR of laccase titrated with azide. Arrow indicates the new signal present at $g = 1.86$ and 8 K.

intensity of this MCD feature is plotted as a solid line in Figure 20C. The 500-nm absorption band has a corresponding low-temperature MCD signal; thus it must be associated with azide binding to the paramagnetic type 2 center. There is also an MCD signal in the region of the 400-nm absorption band; however, it does not exhibit the same behavior as the absorption intensity (Figure 20B). The 385-nm MCD signal first increases and then decreases in intensity with increasing azide concentration. Its magnitude is plotted as the dot-dash line in Figure 20C. Although the low-temperature MCD signal does not correlate with the 400-nm absorption band, it does correlate with an unusual $g = 1.86$ signal in the EPR spectrum (Figure 20D), which we have shown to be associated with <10% of the type 3 sites that become protonatively uncoupled (and hence paramagnetic) upon binding azide. Thus, the intense 400-nm absorption band has no low-temperature MCD signal associated with it, and it must correspond to azide bound to the MCD-silent coupled type 3 center.

The low-temperature MCD and absorption titration studies (Figure 10) have determined that azide binds to both the type 2 and type 3 centers with similar binding constants. A series of chemical perturbations and stoichiometry studies have shown that these effects are associated with the same azide. This demonstrates that one N_3^- bridges between the type 2 and type 3 centers in laccase. These and other results from MCD spectroscopy first defined the presence of a trinuclear copper cluster active site in biology (89). At higher azide concentration, a second azide binds to the trinuclear site in laccase. Messerschmidt et al. have determined from X-ray crystallography that a trinuclear copper cluster site is also present in ascorbate oxidase (87, 92) and have obtained a crystal structure for a two-azide-bound derivative (87). It appears that some differences exist between the two-azide-bound laccase and ascorbate oxidase derivatives, and it will be important to spectroscopically correlate between these sites.

Having demonstrated that the type 3 center must be viewed as part of a trinuclear copper cluster, including the type 2 center, it was important to determine which coppers are required for the reactivity of the multicopper oxidases with dioxygen. We had already demonstrated using X-ray absorption edges (Figure 16C) that a reduced type 3 center in the presence of an oxidized type 1 center does not react with O_2 (85, 86). We next looked at the reactivity of the fully reduced T2D [T1_{red} T3_{red}] derivative with O_2 . This had been generally viewed as the combination of copper centers in laccase required for dioxygen reactivity in the mechanistic proposals in the literature (93, 94). From Figure 21A it is clear that the 8984-eV-reduced Cu K-edge peak does not change on exposure of fully reduced T2D laccase to O_2 . This indicates that the type 2 center is required for dioxygen reactivity. Thus, the Cu K-edge

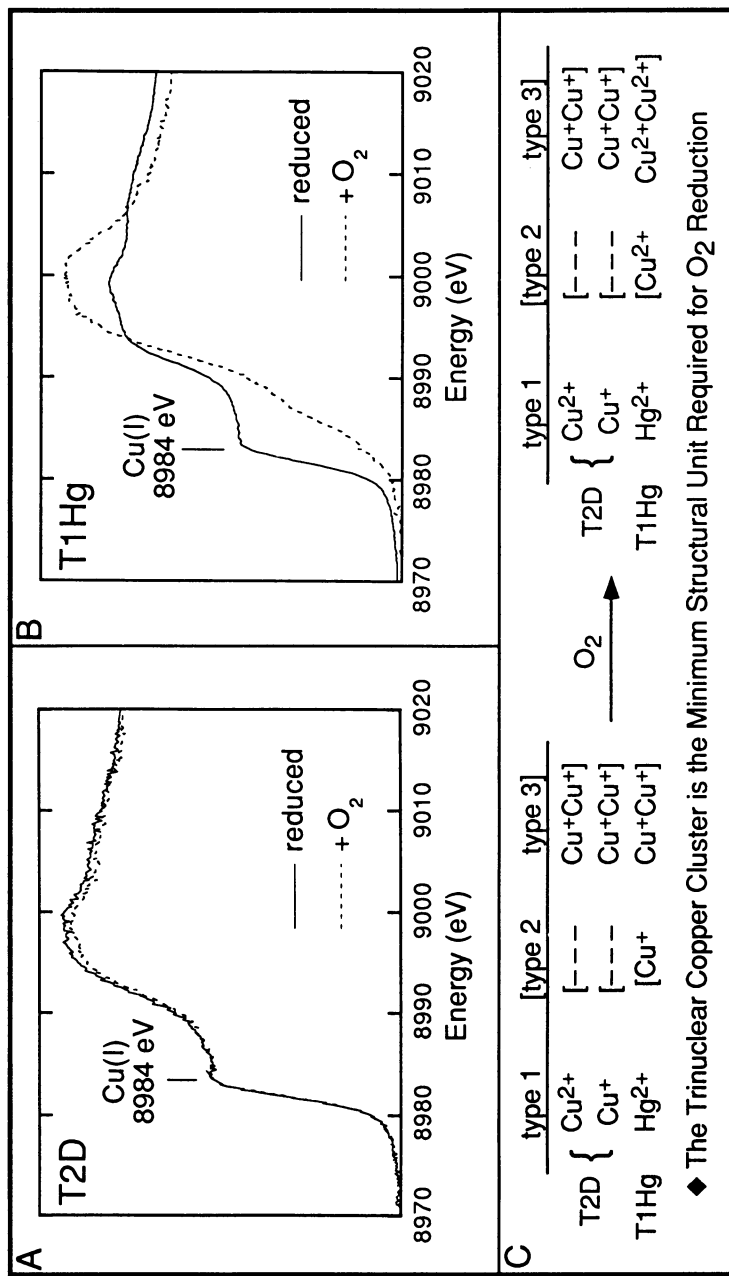


Figure 21. Laccase copper centers required for dioxygen reactivity. A: XAS of fully reduced T2D laccase and fully reduced T2D laccase following exposure to dioxygen. B: XAS of reduced T1Hg laccase and reduced T1Hg laccase following exposure to dioxygen. C: Summary of the reactivity of deoxy T2D, fully reduced T2D, and reduced T1Hg laccase with oxygen.

spectra of the T1Hg derivative, which contains a valid type 2/type 3 trinuclear copper cluster, was investigated. From Figure 21B, the fully reduced trinuclear copper cluster site rapidly reacts with O₂ eliminating the 8984-eV peak. Thus, the trinuclear copper cluster is the minimum structural unit required for O₂ reduction (95).

Because the mercuric ion in T1Hg laccase is redox inactive, this derivative has one less electron equivalent available for O₂ reduction than native laccase. This property enabled us to stabilize an oxygen intermediate in T1Hg laccase. A combination of low-temperature MCD and XAS has demonstrated that two coppers of the trinuclear cluster are oxidized in this intermediate (41). Thus, two electrons have been transferred to dioxygen and this species corresponds to a peroxide level intermediate that can be compared to the peroxy-binuclear cupric sites in oxyhemocyanin and oxytyrosinase. As is clear from Figure 22A, the peroxide intermediate in laccase has a strikingly different charge-transfer spectrum from that of oxyhemocyanin and oxytyrosinase. This requires a different geometric and electronic structure for this peroxy-trinuclear copper cluster site (41). Detailed spectral studies on this intermediate are presently underway (Shin, W.; Cole, J. L.; Root, D. E.; Solomon, E. I., unpublished results). However, at this point our data indicate that it corresponds to a hydroperoxide bound end-on to one of the coppers of an oxidized type 3 center and also likely bridging to a reduced type 2 copper center (Figure 22B). Messerschmidt et al. have since obtained a crystal structure of a low-affinity peroxide-bound adduct of ascorbate oxidase that is also described as having hydroperoxide end-on bound to one of the type 3 coppers. (This peroxide adduct has the three coppers of the trinuclear cluster unbridged and therefore uncoupled in contrast to the oxygen intermediate of T1Hg laccase.) The oxygen intermediate of T1Hg laccase indicates the mechanistic relevance of a end-on hydroperoxide-bound form of the protein. This difference in peroxide binding relative to hemocyanin and tyrosinase appears to play a key role in stabilizing the peroxide intermediate and promoting its irreversible further reduction to water at the trinuclear copper cluster site.

Summary

At this point the unique spectral features associated with the major classes of active sites in copper proteins are reasonably well understood and define active site electronic structures that provide significant insight into their reactivities in biology. For the blue copper sites, we determined that the unique spectral features derive from a ground-state wave function that has a high anisotropic covalency involving the thiolate ligand. This covalency provides a very efficient superexchange pathway

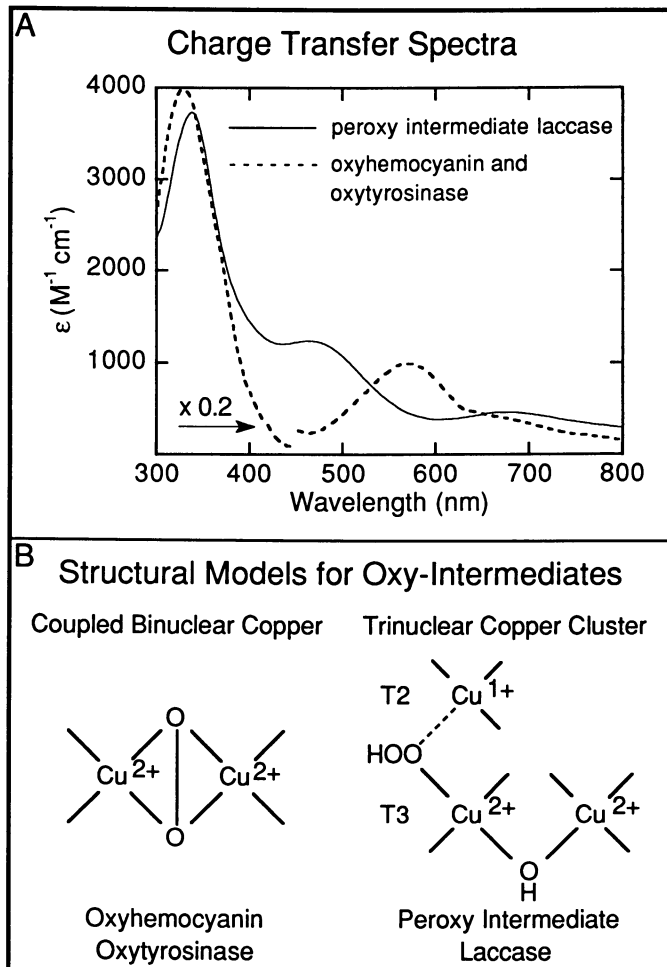


Figure 22. Comparison of oxygen intermediates. A: Electronic absorption spectra of the peroxy-intermediate in laccase versus oxyhemocyanin and oxytyrosinase. B: Proposed structural differences between peroxide binding in oxyhemocyanin and oxytyrosinase relative to the end-on bound hydroperoxide intermediate at the trinuclear copper cluster in laccase.

for long-range electron transfer. For the coupled binuclear copper active sites, we have seen that the unique spectral features of the oxy site correspond to a new bridging peroxide electronic structure that has very strong σ -donor and π -acceptor properties. These properties appear to make significant contributions to the reversible binding and activation of dioxygen by these active sites. In the multicopper oxidases, our spec-

tral studies determined that the type 3 center is fundamentally different from the coupled binuclear copper site in hemocyanin and tyrosinase, that it is part of a trinuclear copper cluster, and that this trinuclear copper cluster is the structure required for O₂ reduction. We have now characterized a peroxide level intermediate at this trinuclear copper cluster site that is strikingly different from the peroxide bound in oxyhemocyanin and oxytyrosinase in that it is bound end-on as hydroperoxide. Our spectral studies presently underway should provide important insight into the geometric and electronic structure differences that are indicated by these spectral differences and their contribution to differences in biological function.

Acknowledgments

This research was supported by the National Science Foundation (CHE-9217628) for the blue copper studies and by the National Institutes of Health (DK-31450) for the coupled binuclear and multicopper oxidase studies. Edward I. Solomon expresses his sincere appreciation to all his students and collaborators who are listed as co-authors in the references for their commitment and contributions to this science.

References

1. Solomon, E. I.; Penfield, K. W.; Wilcox, D. E. *Struct. Bonding* **1983**, *53*, 1–57.
2. Solomon, E. I.; Baldwin, M. J.; Lowery, M. D. *Chem. Rev.* **1992**, *92*, 521–542.
3. Solomon, E. I.; Lowery, M. D. *Science (Washington, D.C.)* **1993**, *259*, 1575–1581.
4. Solomon, E. I.; Lowery, M. D. In *The Chemistry of Copper and Zinc Triads*; Welch, A. J.; Chapman, S. K., Eds.; The Royal Society of Chemistry: Cambridge, England, 1993; pp 12–29.
5. Solomon, E. I.; Hemming, B. L.; Root, D. E. In *Bioinorganic Chemistry of Copper*; Karlin K. D.; Tyeklár, Z., Eds.; Chapman & Hall: New York, 1992; pp 3–20.
6. Solomon, E. I. *Comments Inorg. Chem.* **1984**, *3*, 225–320.
7. Ballhausen, C. J. *Introduction to Ligand Field Theory*; McGraw-Hill: New York, 1962.
8. McClure, D. S. *Electronic Spectra of Molecules and Ions in Crystals*; Academic: New York, 1959.
9. Griffith, J. S. *The Theory of Transition Metal Ions*; Cambridge University Press: London, 1964.
10. Sugano, S.; Tanabe, Y.; Kamimura, H. *Multiplets of Transition Metal Ions in Crystals*; Academic: New York, 1970.
11. Figgis, B. N. *Introduction to Ligand Fields*; Interscience: New York, 1967.
12. Hitchman, M. A.; Cassidy, P. J. *Inorg. Chem.* **1979**, *18*, 1745–1754.
13. Johnson, K. H. *Adv. Quantum Chem.* **1973**, *7*, 143–185.
14. Johnson, K. H.; Norman, J. G., Jr.; Connolly, J. W. D. In *Computational Methods*

- for Large Molecules and Localized States in Solids; Herman, F.; McLean, A. D.; Nesbet, R. K., Eds.; Plenum: New York, 1973; pp 161–201.
- 15. Connolly, J. W. D. In *Semiempirical Methods of Electronic Structure Calculations, Part A: Techniques*; Segal, G. A., Ed.; Plenum: New York, 1977.
 - 16. Rosch, N. In *Electrons in Finite and Infinite Structures*; Phariseu, P.; Scheire, L., Eds.; Wiley: New York, 1977.
 - 17. Slater, J. C. *The Calculation of Molecular Orbitals*; John Wiley & Sons: New York, 1979; p 104.
 - 18. Gewirth, A. A.; Cohen, S. L.; Schugar, H. J.; Solomon, E. I. *Inorg. Chem.* **1987**, *26*, 1133–1146.
 - 19. Solomon, E. I.; Gewirth, A. A.; Cohen, S. L. In *Understanding Molecular Properties*; Avery, J.; Dahl, J. P.; Hansen, A. E., Eds.; D. Reidel: Dordrecht, Netherlands, 1987; pp 27–68.
 - 20. Didziulis, S. V.; Cohen, S. L.; Gewirth, A. A.; Solomon, E. I. *J. Am. Chem. Soc.* **1988**, *110*, 250–268.
 - 21. Bencini, A.; Gatteschi, D. *J. Am. Chem. Soc.* **1983**, *105*, 5535–5541.
 - 22. Chow, C.; Chang, K.; Willett, R. D. *J. Chem. Phys.* **1973**, *59*, 2629–2640.
 - 23. Solomon, E. I.; Lowery, M. D.; LaCroix, L. B.; Root, D. E. In *Methods in Enzymology*; Riordan, J. F.; Vallee, B. L., Eds.; 1993; Vol. 226, Part C; pp 1–33.
 - 24. Desjardins, S. R.; Penfield, K. W.; Cohen, S. L.; Musselman, R. L.; Solomon, E. I. *J. Am. Chem. Soc.* **1983**, *105*, 4590–4603.
 - 25. Mulliken, R. S.; Rieke, C. A.; Orloff, D.; Orloff, H. *J. Chem. Phys.* **1949**, *17*, 1248–1267.
 - 26. Solomon, E. I.; Hare, J. W.; Gray, H. B. *Proc. Natl. Acad. Sci. U.S.A.* **1976**, *73*, 1389–1392.
 - 27. Guss, J. M.; Freeman, H. C. *J. Mol. Biol.* **1983**, *169*, 521–563.
 - 28. Lowery, M. D.; Guckert, J. A.; Gebhard, M. S.; Solomon, E. I. *J. Am. Chem. Soc.* **1993**, *115*, 3012–3013.
 - 29. Penfield, K. W.; Gay, R. R.; Himmelwright, R. S.; Eickman, N. C.; Norris, V. A.; Freeman, H. C.; Solomon, E. I. *J. Am. Chem. Soc.* **1981**, *103*, 4382–4388.
 - 30. Bates, C. A.; Moore, W. S.; Standley, K. J.; Stevens, K. W. H. *Proc. Phys. Soc.* **1962**, *79*, 73.
 - 31. Sharnoff, M. *J. Chem. Phys.* **1965**, *42*, 3383–3395.
 - 32. Roberts, J. E.; Brown, T. G.; Hoffman, B. M.; Peisach, J. *J. Am. Chem. Soc.* **1980**, *102*, 825–829.
 - 33. Gewirth, A. A.; Solomon, E. I. *J. Am. Chem. Soc.* **1988**, *110*, 3811–3819.
 - 34. Shadle, S. E.; Penner-Hahn, J. E.; Schugar, H. J.; Hedman, B.; Hodgson, K. O.; Solomon, E. I. *J. Am. Chem. Soc.* **1993**, *115*, 767–776.
 - 35. Scott, R. A.; Hahn, J. E.; Doniach, S.; Freeman, H. C.; Hodgson, K. O. *J. Am. Chem. Soc.* **1982**, *104*, 5364–5369.
 - 36. Penfield, K. W.; Gewirth, A. A.; Solomon, E. I. *J. Am. Chem. Soc.* **1985**, *107*, 4519–4529.
 - 37. Norman, J. G. *J. Mol. Phys.* **1976**, *31*, 1191–1198.
 - 38. George, S. J.; Lowery, M. D.; Solomon, E. I.; Cramer, S. P. *J. Am. Chem. Soc.* **1993**, *115*, 2968–2969.
 - 39. Hughey, J. L., IV; Fawcett, T. G.; Rudich, S. M.; Lalancette, R. A.; Potenza, J. A.; Schugar, H. J. *J. Am. Chem. Soc.* **1979**, *101*, 2617–2623.
 - 40. Messerschmidt, A.; Ladenstein, R.; Huber, R.; Bolognesi, M.; Avigliano, L.; Petruzzelli, R.; Rossi, A.; Finazzi-Agro, A. *J. Mol. Biol.* **1992**, *224*, 179–205.

41. Cole, J. L.; Ballou, D. P.; Solomon, E. I. *J. Am. Chem. Soc.* **1991**, *113*, 8544–8546.
42. Jolly, R. L., Jr.; Evans, L. H.; Makino, N.; Mason, H. S. *J. Biol. Chem.* **1974**, *249*, 335.
43. Himmelwright, R. S.; Eickman, N. C.; LuBien, C. D.; Lerch, K.; Solomon, E. I. *J. Am. Chem. Soc.* **1980**, *102*, 7339–7344.
44. Woolery, G. L.; Powers, L.; Winkler, M.; Solomon, E. I.; Spiro, T. G. *J. Am. Chem. Soc.* **1984**, *106*, 86–92.
45. Woolery, G. L.; Powers, L.; Winkler, M.; Solomon, E. I.; Lerch, K.; Spiro, T. G. *Biochim. Biophys. Acta* **1984**, *788*, 155–161.
46. Freedman, T. B.; Loehr, J. S.; Loehr, T. M. *J. Am. Chem. Soc.* **1976**, *98*, 2809–2815.
47. Larrabee, J. A.; Spiro, T. G. *J. Am. Chem. Soc.* **1980**, *102*, 4217–4223.
48. Eickman, N. C.; Solomon, E. I.; Larrabee, J. A.; Spiro, T. G.; Lerch, K. *J. Am. Chem. Soc.* **1978**, *100*, 6529–6531.
49. Solomon, E. I.; Dooley, D. M.; Wang, R.-H.; Gray, H. B.; Cerdonio, M.; Mongo, F.; Romani, G. L. *J. Am. Chem. Soc.* **1976**, *98*, 1029–1031.
50. Dooley, D. M.; Scott, R. A.; Ellinghaus, J.; Solomon, E. I.; Gray, H. B. *Proc. Natl. Acad. Sci. U.S.A.* **1978**, *75*, 3019–3022.
51. Fee, J. A.; Malkin, R. M.; Malmström, B. G.; Vänngård, T. *J. Biol. Chem.* **1969**, *88*, 4200–4207.
52. Volbeda, A.; Hol, W. G. *J. Mol. Biol.* **1989**, *209*, 249–279.
53. Eickman, N. C.; Himmelwright, R. S.; Solomon, E. I. *Proc. Natl. Acad. Sci. U.S.A.* **1979**, *76*, 2094–2098.
54. Karlin, K. D.; Cruse, R. W.; Gultneh, Y.; Farooq, A.; Hayes, J. C.; Zubietta, J. *J. Am. Chem. Soc.* **1987**, *109*, 2668–2679.
55. Pate, J. E.; Cruse, R. W.; Karlin, K. D.; Solomon, E. I. *J. Am. Chem. Soc.* **1987**, *109*, 2624–2630.
56. Pate, J. E.; Ross, P. K.; Thamann, T. J.; Reed, C. A.; Karlin, K. D.; Sorrell, T. N.; Solomon, E. I. *J. Am. Chem. Soc.* **1989**, *111*, 5198–5209.
57. Ross, P. K.; Allendorf, M. D.; Solomon, E. I. *J. Am. Chem. Soc.* **1989**, *111*, 4009–4021.
58. Tuczek, F.; Solomon, E. I. *Inorg. Chem.* **1993**, *32*, 2850–2862.
59. Solomon, E. I.; Tuczek, F.; Root, D. E.; Brown, C. A. *Chem. Rev.* **1994**, *92*, 827–856.
60. Tuczek, F.; Solomon, E. I. *J. Am. Chem. Soc.* **1994**, *116*, 6916–6924.
61. Sorrell, T. N.; O'Connor, C. J.; Anderson, O. P.; Reibenspies, J. H. *J. Am. Chem. Soc.* **1985**, *107*, 4199–4206.
62. McKee, V.; Dagdigian, J. V.; Bau, R.; Reed, C. A. *J. Am. Chem. Soc.* **1981**, *103*, 7000–7001.
63. McKee, V.; Zvagulis, M.; Dagdigian, J. V.; Patch, M. G.; Reed, C. A. *J. Am. Chem. Soc.* **1984**, *106*, 4765–4772.
64. Karlin, K. D.; Cohen, B. I.; Hayes, J. C.; Farooq, A.; Zubietta, J. *Inorg. Chem.* **1987**, *26*, 147–153.
65. Kitajima, N.; Fujisawa, K.; Moro-oka, Y.; Toriumi, K. *J. Am. Chem. Soc.* **1989**, *111*, 8975–8976.
66. Kitajima, N.; Fujisawa, K.; Fujimoto, C.; Moro-oka, Y.; Hashimoto, S.; Kitagawa, T.; Toriumi, K.; Tatsumi, K.; Nakamura, A. *J. Am. Chem. Soc.* **1992**, *114*, 1277–1291.
67. Magnus, K.; Ton-That, H. *J. Inorg. Biochem.* **1992**, *47*, 20.
68. Ross, P. K.; Solomon, E. I. *J. Am. Chem. Soc.* **1990**, *112*, 5871–5872.
69. Ross, P. K.; Solomon, E. I. *J. Am. Chem. Soc.* **1991**, *113*, 3246–3259.

70. Noddleman, L.; Norman, J. G., Jr. *J. Chem. Phys.* **1979**, *70*, 4903.
71. Noddleman, L. *J. Chem. Phys.* **1981**, *74*, 5737–5743.
72. Baldwin, M. J.; Ross, P. K.; Pate, J. E.; Tyeklar, Z.; Karlin, K. D.; Solomon, E. I. *J. Am. Chem. Soc.* **1991**, *113*, 8671–8679.
73. Baldwin, M. J.; Root, D. E.; Pate, J. E.; Fujisawa, K.; Kitajima, N.; Solomon, E. I. *J. Am. Chem. Soc.* **1992**, *114*, 10421–10431.
74. Jacobson, R. R.; Tyeklar, Z.; Farooq, A.; Karlin, K. D.; Liu, S.; Zubietta, J. *J. Am. Chem. Soc.* **1988**, *110*, 3690–3692.
75. Cole, J. L.; Clark, P. A.; Solomon, E. I. *J. Am. Chem. Soc.* **1990**, *112*, 9534–9548.
76. Malmström, B. G. In *New Trends in Bio-inorganic Chemistry*; Williams, R. J. P.; DaSilva, R. J. R. F., Eds.; Academic: London, 1978; pp 59–78.
77. Fee, J. A. *Struct. Bonding* **1975**, *23*, 1–60.
78. Reinhamar, B. In *Copper Proteins and Copper Enzymes*; Lontie, R., Ed.; CRC Press: Boca Raton, 1984; Vol. III; pp 1–31.
79. Finazzi-Agro, A. *Life Chem. Rep.* **1987**, *5*, 199–209.
80. Ryden, L. In *Copper Proteins and Copper Enzymes*; R. Lontie, Ed.; CRC Press: Boca Raton, 1984; Vol. III.
81. Graziani, M. T.; Morpurgo, L.; Rotilio, G.; Mondovi, B. *FEBS Lett.* **1976**, *70*, 87–90.
82. Morie-Bebel, M. M.; Morris, M. C.; Menzie, J. L.; McMillin, D. R. *J. Am. Chem. Soc.* **1984**, *106*, 3677–3678.
83. Reinhamar, B. R. M. *Biochim. Biophys. Acta* **1972**, *275*, 245–259.
84. Spira-Solomon, D. J.; Solomon, E. I. *J. Am. Chem. Soc.* **1987**, *109*, 6421–6432.
85. LuBien, C. D.; Winkler, M. E.; Thamann, T. J.; Scott, R. A.; Co, M. S.; Hodgson, K. O.; Solomon, E. I. *J. Am. Chem. Soc.* **1981**, *103*, 7014–7016.
86. Kau, L.-S.; Spira-Solomon, D. J.; Penner-Hahn, J. E.; Hodgson, K. O.; Solomon, E. I. *J. Am. Chem. Soc.* **1987**, *109*, 6433–6442.
87. Messerschmidt, A. *Adv. Inorg. Chem.* **1993**, *40*, 121–185.
88. Westmoreland, T. D.; Wilcox, D. E.; Baldwin, M. J.; Mims, W. B.; Solomon, E. I. *J. Am. Chem. Soc.* **1989**, *111*, 6106–6123.
89. Allendorf, M. D.; Spira, D. J.; Solomon, E. I. *Proc. Natl. Acad. Sci. U.S.A.* **1985**, *82*, 3063–3067.
90. Spira-Solomon, D. J.; Allendorf, M. D.; Solomon, E. I. *J. Am. Chem. Soc.* **1986**, *108*, 5318–5328.
91. Stephens, P. J. *Adv. Chem. Phys.* **1976**, *35*, 197.
92. Messerschmidt, A.; Rossi, A.; Ladenstein, R.; Huber, R.; Bolognesi, M.; Guiseppina, G.; Marchesini, A.; Petruzzelli, R.; Finazzi-Agro, A. *J. Mol. Biol.* **1989**, *206*, 513–529.
93. Reinhamar, B.; Oda, Y. *J. Inorg. Biochem.* **1979**, *11*, 115–127.
94. Farver, O.; Goldberg, M.; Pecht, I. *Eur. J. Biochem.* **1980**, *104*, 71–77.
95. Cole, J. L.; Tan, G. O.; Yang, E. K.; Hodgson, K. O.; Solomon, E. I. *J. Am. Chem. Soc.* **1990**, *112*, 2243–2249.

RECEIVED for review July 19, 1993. ACCEPTED revised manuscript May 10, 1994.